METHOD FOR USING A LASER AND CAMERA TO DETERMINE THE TURBIDITY OF A LIQUID SYSTEM

ELISABETH SMITH

A THESIS SUBMITTED TO THE FACULTY OF GRADUATE STUDIES IN PARTIAL FULFILLMENT OF THE REQUIREMENTS FOR THE DEGREE OF MASTER OF SCIENCE

GRADUATE PROGRAM IN EARTH AND SPACE SCIENCE
YORK UNIVERSITY
TORONTO, ONTARIO

SEPTEMBER 2018

Abstract

The surface of Titan hosts lakes of liquid methane. Evidence suggests the presence of suspended particles in these lakes. A method utilizing a laser and camera to find turbidity is explored. Extinction coefficients were found by measuring the backscatter of light from a laser with a camera. Lasers of various wavelengths were pointed at a specified angle into an aquarium filled with water. Five images are taken of the laser. TiO_2 and SiO_2 particles were incrementally added to the system. Five more images are taken. Images were analyzed to find the extinction coefficient. The change in extinction coefficients against the number concentration of particles was then plotted. This data was fitted to equations, which showed the number concentration of particles could be determined from the observed extinction coefficient.

Acknowledgements

I would first like to thank my adviser, Dr. John Moores, for taking me on as a graduate student. Under his direction, I learned a great deal about space and planetary science. The experience I've gained and knowledge I've learned will be invaluable as I continue my career. I would also like to thank Dr. Regina Lee, who served as a supervisor and as the chair of my defense committee, as well as the other members of my committee, Dr. Patrick Hall and Dr. Mogjan Jadidi.

I would also like to thank my fellow members of the Planetary Volatiles Lab – they've proven to be not just good colleagues, but also great friends. They, too, have taught me a great deal about many different aspects of science. I especially want to thank my Undergraduate assistants Keagan, Romina, Derek, Abteen, Alex, and Jadyn for helping to set up and run experiments. To all of you wonderful folks of PVL, I shall sincerely miss our movie outings! May we meet again for tasty tacos and colorful cocktails!

I also wish to thank 1st LT Jess Weise and 1st LT Laura Curro of the USAF for answering basic organic chemistry questions and sending Game of Thrones memes via Facebook messenger. Additionally, I wish to thank my friend/Dungeon Master Will and friend/party member Melanie, and our fictional mutated pet rat Reginald von Mordecai, for supporting me through boss fights and research alike.

Most of all, I wish to thank my family who supported me throughout my time as a Master's candidate and putting up with my ridiculous home sciencing. I also thank my dog Nightwing for being the snuggliest and goodest of boys. I would also like to dedicate this to my late dog Emerald. May you feast in peace on Subway sandwiches and King's Hawaiian rolls.

Table of Contents

List of Tables

List of Figures

1. Introduction

1.1 History of Titan Exploration

In 1655 Titan, the second largest moon in the solar system, was discovered by Christiaan Huygens. Huygens' discovery of Saturn's satellite would be honored centuries later with the naming of the probe *Huygens*, which would take atmospheric measurements (described in further detail later) as it descended to Titan's surface and for a time afterwards (Zarnecki, McDonnel & Green, 1992). Since then, Titan has been the focus of many astronomers and scientists, who hypothesized about the Titan environment.

In 1908, Spanish astronomer José Comas Solá viewed Titan through a telescope. During his observation, he witnessed limb darkening of the satellite. Limb darkening is an effect where solar light reflected back to Earth from a planet's limb (in this case, the satellite Titan) is darker than that of the central region (Coustenis, 2008). This was the first indication that Titan, like Earth, had an atmosphere.

In the mid 1940's, astronomer Gerard P. Kuiper, using a telescope with a spectrometer, found that Titan had an atmosphere rich in methane (Kuiper, 1944). It would later be suggested that N_2 gas could be present, due to photolysis of NH_3 (ammonia) on Titan (Lewis, 1971). Since Titan is the only other satellite in the solar system that is known to have an atmosphere, interest in the satellite as a potential analogue to Earth increased (Kuiper, 1944; Horst, 2017a).

The first spacecraft to reach Titan was the Pioneer 11 probe. Pioneer 11 was launched in April 1973, and arrived in the Saturnian system in 1979. Pioneer took limb darkening (the effect of decreasing brightness of an object as height from the center increases, due to changes in temperature) and polarization measurements at red and blue wavelengths at a variety of phase

angles, ranging from 15° to 97°, and was able to constrain the size of aerosols to having a diameter of 0.09 μm, assuming a refractive index of 2.0 (Tomasko, 1980). Tomasko also suggested that particle size increases as altitude above the surface decreases.

In November 1980, the Voyager 1 probe passed through the Saturn system and was able to take radio occultation measurements of Titan's atmosphere, measuring properties such as the radius of the planet's surface and scale height, surface pressure and temperature, and identified nitrogen as the primary atmospheric constituent (Tyler et al., 1981), confirming previous findings for the satellite. Analysis of the data found that the satellite has a surface temperature of approximately 95 K, and a surface pressure of approximately 1.5 bar (Lindal & Wood, 1983). This was consistent with measurements from the Infrared Interferometer Spectrometer and Radiometer (IRIS) on the probe (Samuelson & Hanel, 1981). It also took images of Titan at visible wavelengths, but was unable to detect the surface due to the haziness of the atmosphere (Smith, Soderblom & Beebe, 1981). Additionally, Voyager 1 acquired spectral and radiometric data from the atmosphere (Hanel, Conrath & Flaser, 1981) and conducted magnetic field studies, which showed that Titan has a magnetosphere with a bipolar magnetic tail (Ness, Acuna & Lepping, 1981). Lindal & Wood (1983) were also able to measure the number density of gas at different altitudes based on the measured refractivity from the radio occultation measurement, and thus were able to find a pressure profile for the Titan atmosphere, as shown in Figure 1.1:

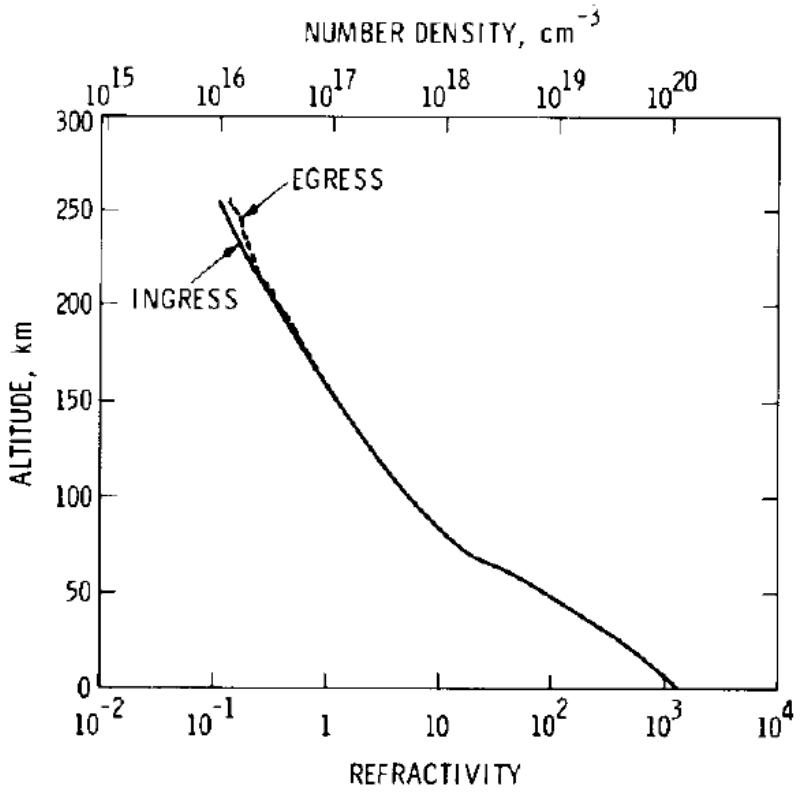

Figure 1.1 - Vertical gas refractivity and number density of gas particles in the atmosphere at different altitudes of Titan (Lindal & Wood, 1983)

These conditions are near the triple point for methane, meaning that it could exist as a liquid, solid or gas (Horst, 2017a). This furthered the argument for Titan as an Earth analogue, as this would mean that Titan would be the only other object in the solar system that is known to have liquid exist in a stable state on its surface. This justified in part another mission to the Saturn system, in the form of a two-part probe, consisting of the *Cassini* orbiter and the *Huygens* lander.

Voyager 2 launched August 20, 1977 and arrived in the Saturnian system in August 1981 (Kohlhase & Penzo, 1977). Voyager 2 made several of the same measurements as Voyager 1 that were in agreement with previous results, such as pressure and temperature (Tyler, Eshleman & Anderson, 1982). Analysis of photopolarimetry data obtained by Voyager 2 found that no single-size spherical particle model accurately describes the polarization that occurred for the atmosphere,

meaning that the aerosols would likely be of various radii (Lane, Hord & West, 1982). Additional images were taken of Titan that showed multiple haze layers and a northern polar "collar" that is dark at short wavelengths (Smith, Soderblom & Batson, 1982).

The Pioneer and Voyager probes obtained significant data of the Titan atomosphere, but they were unable to obtain significant data from the satellite's surface, due to the haze. When the Cassini-Huygens mission was launched in 1997, it was fitted with various instruments that would allow it to study Titan's surface. The RADAR instrument was resposible for finding very smooth features on Titan's surface – these could either be dry lakebeds, or the surfaces of actual lakes (Stofan et al., 2007). However, without further information, it would be difficult to distinguish between the two. Another instrument that was crucial to the discovery of lakes was the Visible and Infrared Mapping Spectrometer (VIMS), as previously mentioned. VIMS was partially responsible for the discovery of lakes on Titan. Since it was able to image in infrared wavelengths, the instrument would not be impeded by the hazey Titanian atmosphere when examining the surface. VIMS captured sunglints off of some of the lakes, as seen in Figure 1.4.1, confirming that liquid does indeed exist on the surface, and not just dry, flat lakebeds (Horst, 2017b). The Huygens probe, of course, had its own suite of surface scientific instruments as well, in addition to the atmospheric intruments it carried. The Science Surface Package (SSP), for example was primarily intended for the determination of physical and chemical propoerties of Titan's oceans (Zarnecki, McDonnel & Green, 1992). The SSP consisted of several sensors that would capture various information, such as a hot wire to determine thermal properties, an Archimedes sensor to determine the density of fluid, and a critical angle refractometer with a photodetector readout to find refractive indices (ESA, 2018). Other instruments on the probe included the Huygens Atmospheric Structure Instrument (Hasi), which measured Titan's atmospheric structure and electrical properties

(Fulchignoni, Ferri & Angrilli, 2002); the Doppler Wind Experiment (DWE), which measured the direction and strength of Titan's zonal winds between the surface and a 160 km altitude (Bird, Dutta-Roy & Heyl, 2003); the Descent Imager/Spectral Radiometer (DISR), an optical intrument taking measurements of the profile of solar heating, the physical properties of aerosol and cloud particles in the atmosphere, composition of the atmosphere, and physical properties and processes of the surface (Tomasko, Doose & Smith, 1996); and the Gas Chromatograph Mass Spectrometer (GCMS), which measured the atmosphere's chemical composition (Niemann, Atreya & Baur, 2002).

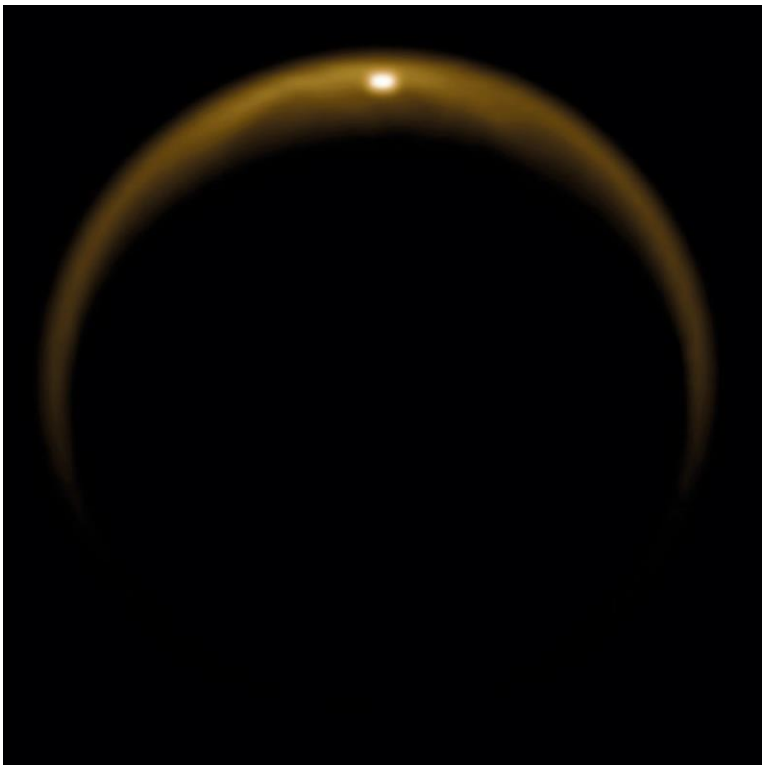

Figure 1.2 – Image of Sunglint from Titan's surface *(Image credit: NASA/JPL/University of Arizona/DLR)*

Several future missions to Titan have been proposed. It has been argued that the only way to reliably determine various properties of Titan's surface and seas is to send a probe to perform in-situ scientific measurements (Mitri & Coustenis, 2014). One such proposed probe is the Titan

Mare Explorer (TiME). This mission was proposed with objectives such as the measurement of sea chemistry, sea depth, constraining of marine processes, determining of sea surface meteorology, and constraining of prebiotic chemistry in the sea (Stofan et al., 2013). The authors suggest using a down-looking echo sounder to determine a number of characteristics, including turbidity (Stofan et al., 2013).

Another proposed mission is the New Frontiers Dragonfly mission. This mission is proposed to land in the Shangri-La organic sand sea, where it would investigate the sands and water ice for prebiotic chemistry, habitability, and biosignatures (Barnes, Turtle & Trainer, 2017). According to Barnes et al., Dragonfly would have a meteorlogical package to measure wind speed and direction, and a microscopic imager that would measure roundness of sand grains, in addition to other instruments that would examine various chemical aspects of the sand.

1.2 Titan's Surface & Lakes

The Cassini-Huygens mission was launched October 15, 1997 from Cape Canaveral (Matson, 2003). It arrived in the Saturnian system in 2004. The Huygens probe landed on the surface of Titan on January 14, 2005 and took data and images during and after its descent (Lebreton et al., 2005). In 2007, the discovery of liquid methane lakes on the surface of Titan was announced, as confirmed by Cassini's RADAR instrument, which found radar-dark patches on Titan's surface during a flyby on July 22, 2006 (Stofan et al., 2007). It was also found that some lakebeds were partly-dry and some liquid filled, suggesting that Titan experiences a hydrological cycle which causes the lakes to fill via rainfall or intersection with a subsurface liquid methane table (Stofan et al., 2007). Figure 1.1 shows a map of Titan from the North pole, obtained with Cassini's RADAR instrument, with the found lakes in dark blue. Since this discovery, the lakes have been the subject of many different studies.

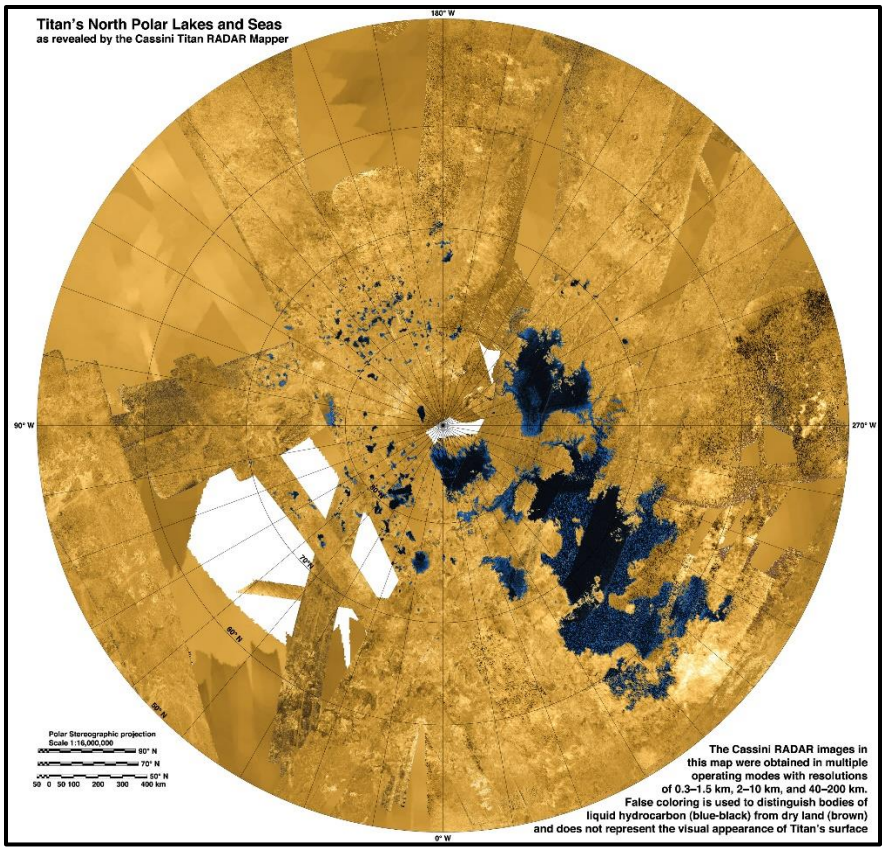

Figure 1.3 – Map of Titan and Lakes (Jet Propulsion Laboratory, 2017)**.** *Data obtained from the Cassini RADAR instrument.*

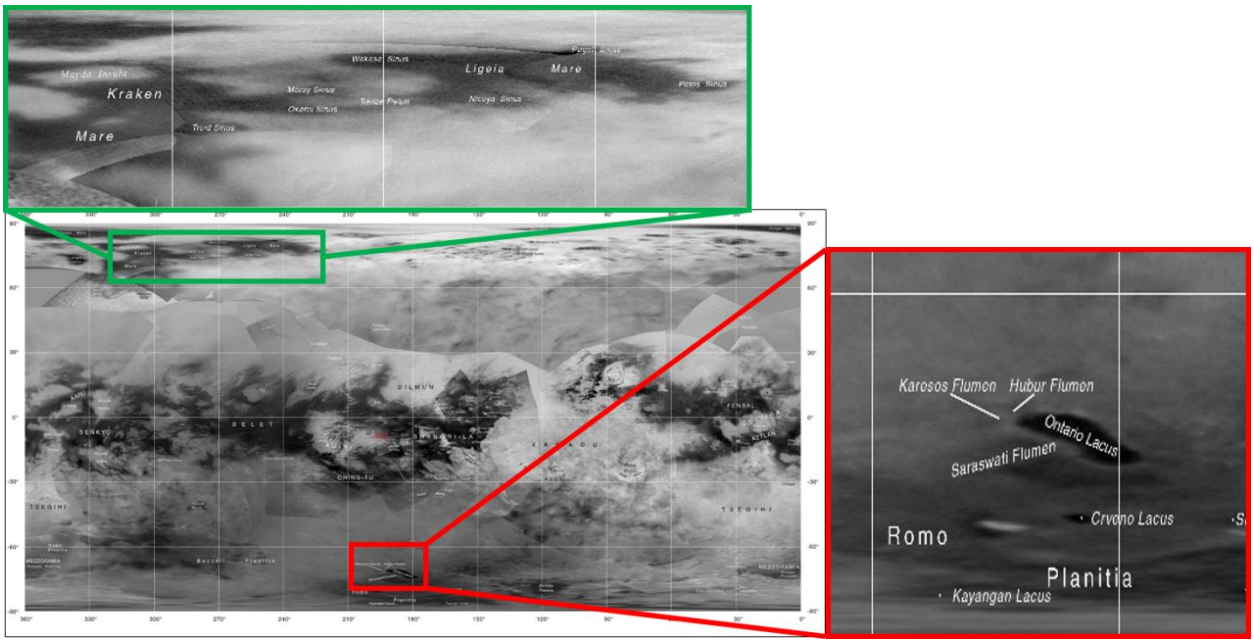

Figure 1.3 – Lakes of Titan. *Kraken Mare and Ligeia Mare are in the northern region of Titan, shown in the green box on top. (Jet Propulsion Laboratory, 2016).*

Observations from the Cassini VIMS instrument of Ontario Lacus, one of the lakes on Titan's surface, shows unusual data from coastal area of the lake (Barnes & Brown, 2009). In Figure 1.4, panel c shows the division of regions by spectral units, where each color represents a different spectral value. Units 1 (blue) and 4 (green) were expected; Units 2 (brown) and 3 (red) were not. Unit 1, representing the lake, was dark at Titan's most transparent wavelengths (1.28 μm, 1.58 μm, 2.0 μm, 2.7 μm, 2.8 μm, 5 μm). Unit 2 was also dark, but not as dark as Unit 1. Unit 3 was bright at 2.0 μm and 5.0 μm. Unit 4 was brightest at 2.0 μm. Barnes and Brown (2009) investigated several possibilities for what may have caused this anomaly in spectral values: first, they examined whether freezing and thawing of ice could have caused this. If the lake were in the process of freezing, then a ring like what is seen in Unit 3 could appear. However, this data was taken during Titan's south polar, 7-year (in Earth years) summer, and thus freezing would be unlikely during this time. They also reject the hypothesis that this is caused by a bathymetry profile

similar to Earth's oceans, as the data presented would suggest a cliff-like drop at the edges of the Unit 2 region, rather than the gradual sloping that would normally be expected. Of the other various hypotheses presented, two likely scenarios are suggested, including the presence of suspended particles from tidal sloshing or the exposure of lake-bottom sediments due to a change in the bulk volume of liquid methane in the lake or tidal forcing (Barnes & Brown, 2009).

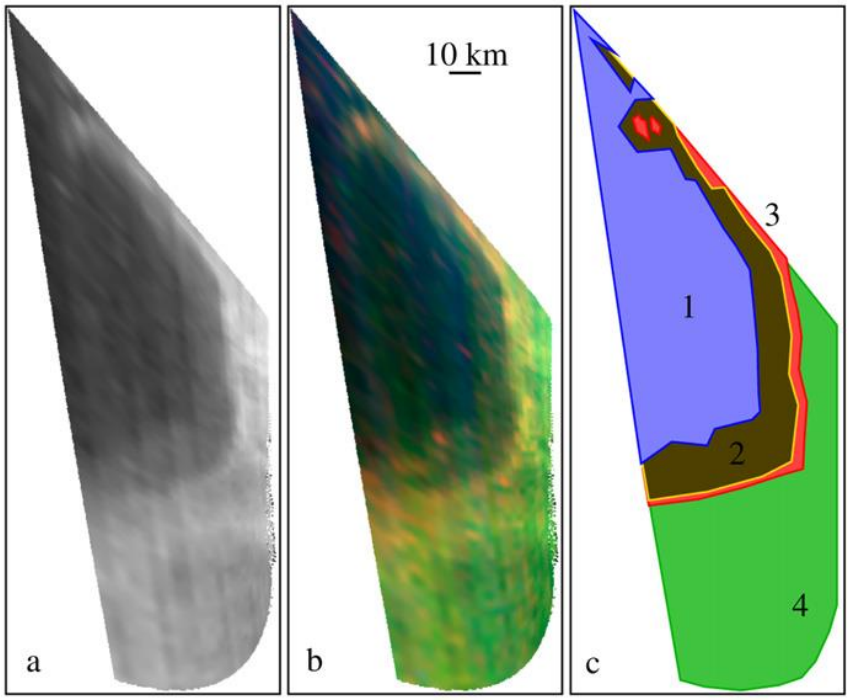

Figure 1.4 – Section of Titan Lake. *In section c, the brown portion labeled as "2' is a section of lake that is suggested to possibly indicate the presence of suspended particles* (Barnes & Brown, 2009)

It has also been suggested that there may be a subsurface supply of liquid methane (Turtle et al., 2018). Cloud activity observed by Cassini showed clouds in the northern polar region appearing sooner than expected, if the activity were purely related to seasonal changes. The clouds also commonly appeared at 60° latitude, suggesting that there may be a subsurface supply of methane there.

1.3 Tholins & Scatterers in Lakes

If the unusual regions identified by Barnes & Brown (2009) were, in fact, due to the presence of particles, what could these particles be? Where could they have come from? A study published in the Journal of Chemical Physics in March 2017 suggests that pockets of acetonitrile (ACN) may be suspended in the methane-dominant lakes (Corrales & Yi, 2017). In this study, Corrales et al. used computer simulations to explore the solvation behavior of ACN in a Titan-like environment. The study found that larger clusters of ACN may be stable in alkane liquids, and that some aggregates of ACN may be suspended if their mass is beneath the required minimum for it to reach terminal velocity in the liquid, as well as in pure methane, ethane and propane solutions (Corrales & Yi, 2017). They also suggest that the precipitation of solid ACN particles formed from large clusters should be investigated (Corrales & Yi, 2017).

Additionally, tholins, which are organic solids made from the plasma irradiation of nitrogen gas and methane gas mixtures, are produced in the atmosphere (McDonald, Thompson & Heinrich, 1994)), and would rain down into the methane lakes. These particles would most likely have an empirical formula of $C_3H_5N_2$ (Sagan, Khare & Lewis, 1984), and would be insoluble in the methane lakes on the surface (McDonald, Thompson & Heinrich, 1994). McDonald, Thompson & Heinrich (1994) were able to verify that such particles could exist. In this experiment, a Tesla coil was placed in a vacuum chamber with gases similar to that of the Titan atmosphere. On Titan, it was hypothesized that the presence of condensable vapours and deposition of solar energy at the surface could result in lightning activity, which would produce the tholins expected (Borucki, McKay & Whitten, 1984). However, no clear evidence of Titan lightning has been identified yet (Fischer & Gurnett, 2011). It should be noted that the lack of detection does not mean that lightning does not occur – rather, it could suggest that the lightning on the satellite is

too weak to be detected by the instruments currently being used to detect it (Kohn & Dujko, 2018). Tholins can also be formed in the upper atmosphere by the dissociation of methane and nitrogen by UV irradiation (Imanaka et al., 2004).

In 2010, a study of Cassini synthetic aperture radar data was published that found a depositional delta at Ontario Lacus, which indicates constant flow along the feeding channel which would transport sediment to the lake (Wall & Hayes, 2010). A recent study using Monte Carlo-based waveform inversion with Cassini VIMS data obtained from Ontario Lacus shows that the lake either has a depth of only a few millimetres (which is physically unlikely) or there is a presence of particles in the lake, floating or suspended, that are scattering light back to Cassini. (Mastroguiseppe & Hayes, 2017).

Interestingly, another liquid body on Titan was studied and was initially believed to be relatively free of any suspended particles. RADAR data from Cassini was used to find that Ligeia Mare is very clear and would contain no more than 0.1% suspended particles (Mastrgiuseppe et al., 2014). However, a more recent study has found repeated transient bright features in Ligeia Mare from multiple observations of the sea (Hofgartner, et al., 2016). The study concludes that the bright features, seen in Figure 1.5, could be the result of floating or suspended particles, bubbles, or waves. Waves are the favored hypothesis of those three, as in similar terrestrial environments, waves occur more commonly than the presence of floating and suspended particles (Hofgartner et al., 2016).

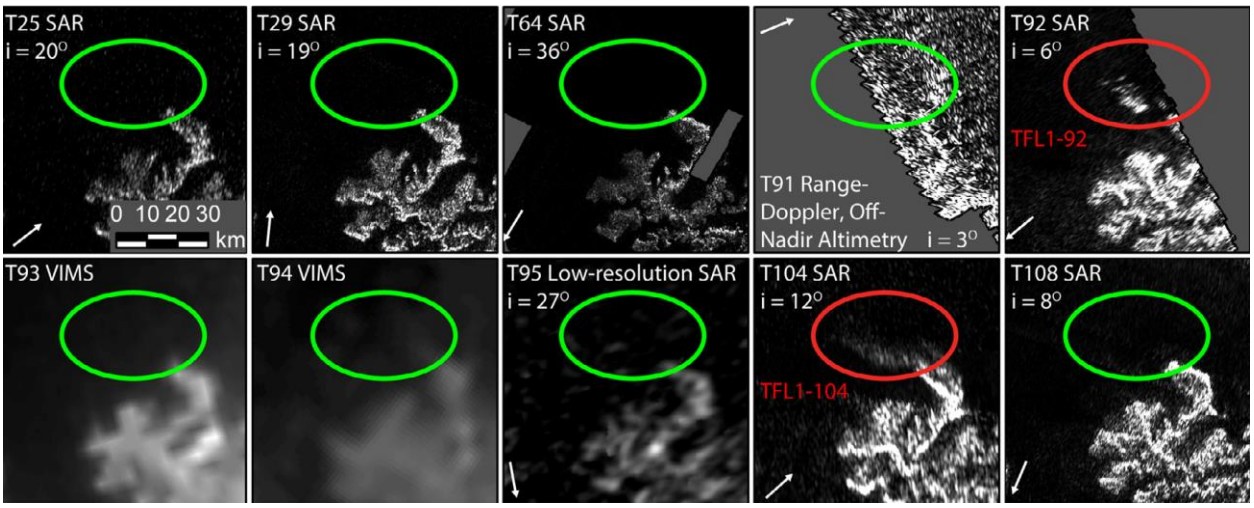

Figure 1.5 – Transient Bright Figures in Ligeia Mare. *Each image is of approximately the same area of Ligeia Mare. The circled portions are where the transient bright features appear (the red circles indicate where the features do appear, and green indicates frames of the same region where the features did not appear).*

In a 2014 study, these authors suggested that thermal disturbances could cause the liquid of the lakes or the particles of the sea floor to separate through exsolution (where a solid solution separates into two different phases) into gases, which could result in the formation of bubbles that could rise to the surface and cause the transient features, and that low-density solids, such as polyacetylene, could also be the particles that are suspended (Hofgartner et al., 2014). An earlier study from the same author also found that ice can form and float in the lakes, and sink to the bottom (Hofgartner & Lunine, 2012). Ice was modeled in the lakes and from the resulting analysis, it was found that different temperatures, varying by season, can cause the ice to sink or float in the lakes (Hofgartner & Lunine, 2012). Additionally, micron sized atmospheric fallout particles or evaporative products is another possibility (Hayes, et al., 2008), consistent with the idea of tholins raining into the lakes.

1.4 Measuring Turbidity

In a mission to one of these lakes, the presence of any such particles could be detected by measuring the turbidity. Turbidity is the “muddiness” or “lack of clarity” that occurs in liquid due to the presence of suspended particles that scatter light (Kirk, 1985). Measurement of turbidity is usually done with a nephelometer (also called a turbidimeter), which measures the intensity of light scattered by the presence of suspended, insoluble particles, and from this intensity, can determine the concentration of such particles (BMG LABTECH, 2017). “Desktop” turbidimeters, which analyze samples obtained from the field in a laboratory, generally operate by detecting the amount of scattered light from a source that passes through the medium being measured, with the light beam forming an angle that is generally 90 degrees or less from the detector (Bin Omar & Bin MatJafri, 2009). A common “in situ” method for measuring turbidity involves the use of a Secchi disk, which is a black and white disk that is lowered into a body of water until the point where it disappears from view; the turbidity of the water is determined from the depth at which it disappears (Priesendorfer, 1986).

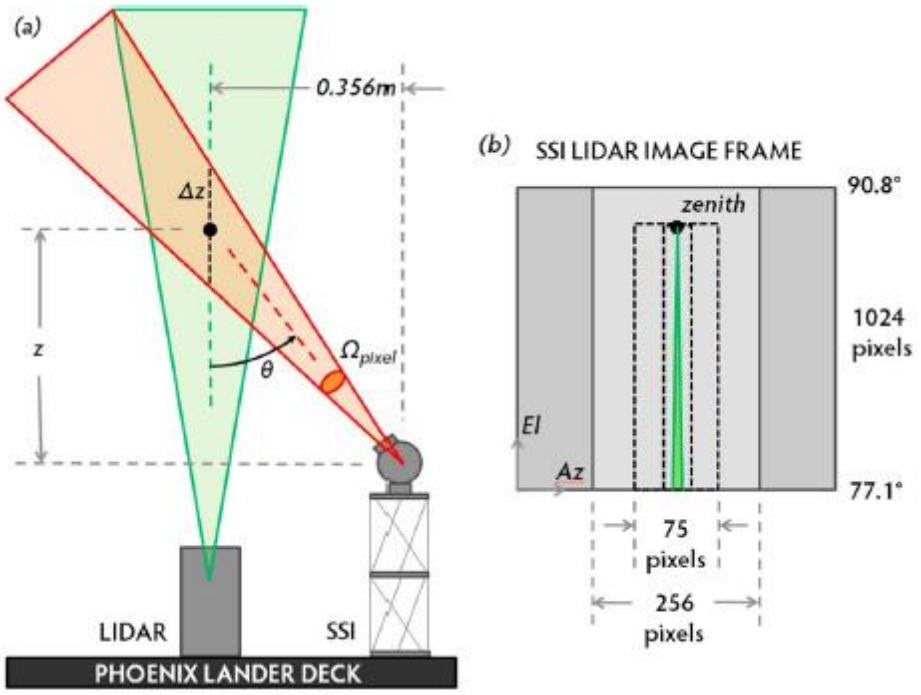

Figure 1.7 – Phoenix Lander Experiment and Analysis. *(a) is an illustration of the setup, where the green is the LIDAR beam and the orange is the camera field of view. (b) shows the analysis, where a box around the beam is taken and analyzed* (Moores & Komguem, 2011).

Moores et al. used a LIDAR instrument onboard the Martian Phoenix lander to measure the ice water content of Martian fog (Moores & Komguem, 2011). To accomplish this, they imaged the LIDAR using Phoenix's Surface Stereo Imager, a camera mounted on a mast of the lander that took high resolution images of the Martian surface and atmospheric clouds (University of Arizona, 2018). Images obtained by the SSI were analyzed to find the ice water content, as illustrated in Figure 1.7.

Lidar and turbidimeters are two of the most common ways for measuring turbidity. However, each has its own drawbacks. Turbidimeters measure the clarity of a system using the Nephelometric Turbidity Unit, which does not correspond to a value representative of the number concentration of particles in a system (that is, the number of particles per unit volume). Additionally, a system that would use a Secchi disk would be complicated by the need for a system

to lower the disk. Lidar could more accurately measure the number of particles in a system, as seen with Moores & Komguem's (2011) research. However, these systems often require larger amounts of energy – for example, the Lidar on the Phoenix lander had an output of 40 mW of energy at 532 nm (Whiteway, et al., 2008). The method proposed in this research would have a much lower energy requirement, with just a 4.5 mW laser.

1.5 Study Parameters and Limitations

The goal of this study is to develop a method of measuring turbidity and/or extinction, for use in the methane lakes of Titan. However, the parameters of the research conducted are not representative of the Titan environment. In this study, the liquid medium used is simple tap water. As such, the optical properties represented in the research may not be representative of the optical properties that could be expected on Titan. For example, liquid methane has a refractive index of approximately1.273 (Martonchik & Orton, 1994)); water has a refractive index of approximately 1.33 (Hale & Querry, 1973).

Additionally, the particles used in this research are not what would be expected in the Titan environment. In this research TiO_2 and SiO_2 are used. These were chosen because they are insoluble in water, readily available in fine particle sizes, and have a large difference in refractivity. On Titan, however, the particles encountered would likely be nitrogen based particles, such as the previously described tholins (Sagan, Khare, & Lewis, 1984) or acetonitrile (Corrales & Yi, 2017). Similarly, as with the liquid media, these particles would likely exhibit different optical and physical properties, such as reflectivity and absorptivity, than that of TiO_2 and SiO_2. SiO_2 has a refractive index range of approximately 1.457 to 1.470 for the laser wavelengths used in this study (Malitson, 1965). TiO_2 has a much higher refractive index – its index ranges between approximately 2.86 and 3.14 at the same wavelengths (DeVore, 1951). Tholins were found to have

a refractive index between 1.68 + 0.0083*i* and 1.72 + 0.06*i* *at* these wavelengths (Khare & Sagan, 1984). This range is comparable to that of the SiO_2, though the addition of the imaginary parts makes tholins unlike the other two particles – the imaginary part suggests that the particles will also absorb some of the light, not just refract it.

If we compare the refractive indices of these two particles against those of the tholins, we can draw a stronger parallel between SiO_2 and the tholins, as they have more similar values. The refractive indices of tholins are much closer to that of SiO_2 than TiO_2. Additionally, the change in refractive indices across the three specified wavelengths are smaller for the tholins, similar to the SiO_2 particles. This suggests that the SiO_2 data is a good analogue for the tholins. However, there is a difference in the refractive indices – unlike the two particles used, the tholin refractive indices contain an imaginary component. As will be seen further on, this will have an impact on the Mie scattering efficiencies.

Another consideration is that the particle sizes may be different. The SiO_2 particles used have a diameter of approximately 2 μm and the TiO_2 particles are in the range of 1 to 2 μm. Laboratory experiments, where tholins were produced in a simulated Titan-like environment have found that the tholins may have a diameter range of approximately 0.2 μm to 2.5 μm, with most particles between 0.5 to 1.5 μm (Szopa et al., 2005). These ranges intersect with the ranges of diameter for TiO_2 and SiO_2, but the overall range is larger.

The particle densities will also factor into the experimental analysis. Although the same mass of particles was added in each increment, the particle densities will vary. SiO_2 has a particle density of 2.0 g/cm^3, and TiO_2 has a density of 4.23 g/cm^3 (Alfa Aesaer, 2018). For Titan tholins, the particle density may change with respect to the pressure the tholin was formed at. For example,

at 40 Pa, tholins may have a particle density of 1.38 g/cm^3, and at 150 Pa, they may have a density of 1.27 g/cm^3 (Sekine et al., 2007).

Although the experiments performed are not necessarily representative of the conditions that would be encountered on Titan's surface, the same principles apply. Parameters such as particle size, refractive index and laser wavelength can all be taken into account when applying this method. The following table summarizes these parameters for the different particles:

Particle	Diameter (μm)	Particle Density (g/cm^3)	Refractive Index (451.9 nm)	Refractive Index (514.3 nm)	Refractive Index (638.0 nm)
SiO_2	2	2.0	1.466	1.462	1.457
TiO_2	1 – 2	4.23	3.14	3.007	2.87
Tholin	0.5 – 1.5	1.27 – 1.38	1.72 +0.06*i*	1.7 + 0.023*i*	1.68 + 0.0083*i*

Table 1.1 - Properties of Scatterers.

For SiO_2 and TiO_2, the imaginary components (which accounts for absorption) are negligible and not included. With the available information, a method to experimentally determine the turbidity of any system can be devised – particularly that of Titan. This research will show that the turbidity can be determined and predicted for any input parameters, whether those parameters represent Earth or Titan.

1.6 Research Objective

This project proposes an alternative method to for finding the turbidity of a methane lake on Titan for a future drone mission. Being able to detect turbidity could verify whether or not there are particles suspended in the lakes as previous studies have suggested, and could offer insight into the overall composition of these lakes, as well as the depth of any mixing that occurs. It could also offer insight into flow from channels, such as the delta found at Ontario Lacus, and possibly provide more insight about the possibility of subsurface methane supplies. This method would be a low-energy and effective alternative to existing technologies.

2. Methodology

2.1 Background Theory

This project uses a CCD camera to capture images of the light backscattered from suspended particles illuminated by a laser beam. A CCD, or charge couple device, is a device that captures images through the detection of photons. When a photon hits the surface of the CCD, it will hit one of the smaller subdivisions of the device, called a pixel. Pixels are composed of a gate, insulating layers, an epitaxial layer (made from silicon and other elements), and a substrate layer made from silicon (Spectral Instruments Inc., 2018). When a photon strikes the pixel, it will create photoelectrons in the epitaxial layer. The gate holds a positive charge that attracts electrons. The insulating layers hold the electrons in place. A time-variable voltage sequence is then used to shift the stored electrons to an output amplifier, which converts the charge to a voltage that can be converted to an image via computer (Lesser, 2015).

In the context of this research, the photons that reach the CCD of the camera being used arrive from backscattering against particles in the medium, due to a phenomenon called Mie scattering. Mie scattering occurs when light is scattered off of a particle that is comparable in size to the wavelength of the light scattered (Andrews, 2000). With backscatter, the light is scattered backwards towards the source. For this research, these backscattered photons will scatter back to the camera CCD, where they will be processed an analyzed to estimate the extinction of the system. Extinction is described as the loss of energy from an incoming photon, as a result of the absorption or scattering by particles (Andrews, 2000). The extinction of light can be used to measure the number of particles in a system, if the size of the particles and other parameters are known. The extinction of light can be measured with the extinction coefficient. We can find this with the Beer-Lambert Law:

$$I(x) = I_0 * e^{(-\eta d)} \quad (1)$$

In this equation, I is the irradiance (W/m^2) in the direct or the transmitted beam, η is the extinction coefficient, and d is the distance along the beam. The above equation would tell us how much light passes through the medium as it travels in the beam direction – however, we then need to consider how much travels back to the camera through backscattering. Therefore, our equation becomes:

$$I(x) = I_0 * e^{(-\eta(d_1+d_2))} \quad (3)$$

Where d_1 is the distance traveled along the beam, and d_2 is the distance traveled from point d_1 to the lens of the camera.

I_0 is the initial irradiance of the laser, found by

$$I_o = \frac{Laser\ Power}{Beam\ Cross\ Section} \quad (4)$$

Using equation 4, we can find I_0 values for each laser used in this research:

	451.9 nm (Blue)	**514.3 nm (Green)**	**638 nm (Red)**
Power	4.5 mW	4.5 mW	4.5 mW
Beam Cross Section Area	1.01×10^{-5} m^2	2.46×10^{-5} m^2	1.41×10^{-5} m^2
Irradiance	895.25 W/m^2	366.34 W/m^2	636.62 W/m^2

Table 2.1 – Laser Irradiances

Because the particles in this system are small, Mie scattering is considered. To account for this, we need to use Mie efficiency coefficients, or Q. Mie efficiency coefficients are the ratio of the particle's scattering cross sections to the projected area of the scattering sphere (Nussenzveig & Wiscombe, 1980). These can be calculated from the following equations (Van de Hulst, 1957; Kerker, 1969; Matzler, 2002):

$$Q_{ext} = \frac{2}{x^2}\sum_{n=1}^{\infty}(2n+1)Re(a_n + b_n) \quad (5)$$

$$Q_{sc} = \frac{2}{x^2}\sum_{n=1}^{\infty}(2n+1)(|a_n|^2 + |b_n|^2) \quad (6)$$

$$Q_b = \frac{1}{x^2}\left|\sum_{n=1}^{\infty}(2n+1)(-1)^n(a_n - b_n)\right|^2 \quad (7)$$

Where Q_{ext} is the extinction efficiency, Q_{sc} is the scattering efficiency, and Q_b is the backscatter efficiency. In these equations, x is the size parameter, calculated by

$$x = \frac{\frac{4}{3}\pi r^3}{\lambda} \quad (8)$$

Where λ is the wavelength of the scattered light. a_n and b_n are Mie coefficients that are dependent on x and the complex refractive index (Wiscombe, 1980). These can be computed as follows (Bohren & Huffman, 1983):

$$a_n = \frac{\mu m^2 j_n(mx)[xj_n(x)]' - \mu_1 j_n(x)[mxj_n(mx)]'}{\mu m^2 j_n(mx)\left[xh_n^{(1)}(x)\right]' - \mu_1 h_n^{(1)}(x)[mxj_n(mx)]'} \quad (9)$$

$$b_n = \frac{\mu_1 j_n(mx)[xj_n(x)]' - \mu j_n(x)[mxj_n(mx)]'}{\mu_1 j_n(mx)\left[xh_n^{(1)}(x)\right]' - \mu h_n^{(1)}(x)[mxj_n(mx)]'} \quad (10)$$

In these equations, m is the refractive index of the sphere relevant to the ambient medium, and the functions $j_n(z)$ and $h_n^{(1)}(z)$ are spherical Bessel functions calculated by (Matzler, 2002):

$$j_n(z) = \sqrt{\frac{\pi}{2z}}J_{n+0.5}(z) \quad (11)$$

$$h_n^{(1)}(z) = j_n(z) + iy_n(z) \quad (12)$$

where

$$y_n(z) = \sqrt{\frac{\pi}{2z}} Y_{n+0.5}(z) \quad (13)$$

$J_{n+0.5}(z)$ and $Y_{n+0.5}(z)$ are Bessel functions of the first and second kind, respectively (Matzler, 2002). A Bessel function of the first kind can be written as

$$J_v(z) = \sum_{k=0}^{\infty} \frac{(-1)^k \left(\frac{x}{2}\right)^{v+2k}}{k!\,(v+k)!} \quad (14)$$

where v is the order of the function (Culham, 2004). A Bessel function of the second kind is written as

$$Y_v(x) = \frac{J_v(x)\cos(v\pi) - J_{-v}(x)}{\sin(v\pi)} \quad (15)$$

In the Titan atmosphere, it was found that Mie scattering was able to reproduce the polarimetry, limb darkening, and photometry data obtained from Pioneer 11 much better than Rayleigh scattering theory, which accounts for the scattering of light by particles much smaller than the wavelength of the scattered light (Tomasko & Smith, 1982). If these particles are raining into the methane lakes on the surface, then it would follow to use Mie scattering theory for the study of turbidity in the lakes, as well.

To account for the effects of Mie scattering, we can multiply the Beer-Lambert Law, as found in equation 3, by the Mie efficiency coefficients for extinction and backscatter, as found in equations 5 and 7. Therefore, the final equation we get for analysis of images is

$$I(x) = I_0 * Q_b * Q_{ext} * e^{(-\eta(d_1+d_2))} \quad (16)$$

In our analysis, the extinction coefficient, η, will include extinction from both the scattering particles and the water. Extinction from the water will remain constant, while the extinction from the scattering particles will change with the increase in particles. Since the

change in the extinction coefficient is the of greater interest than the value of the extinction coefficient, the constant extinction coefficient from the water can be ignored.

The error for the experimental analysis is calculated by

$$e_{total} = \sqrt{e_1^2 + e_2^2 + \cdots + e_n^2} \quad (17)$$

Where *e* is an error, as a percentage. Error sources include the mass measurement of particles added (with 2.0% error), volume of the liquid in the aquarium (2.2% error), and the distance values for both the length along the beam and distance back to the camera (4.14% error). The uncertainty for equation 16 can be found with

$$e_{I(x)} = \left[-(d_1 + d_2) * I_0 * Q_b * Q_{ext} * e^{(-\eta(d_1+d_2))}\right]^2 + 2\left[\left(-\eta * I_o * Q_b * Q_{ext} * e^{(-\eta(d_1+d_2))}\right)\right] \quad (18)$$

The mass of particles added was measured with a digital scale, with a target value of 0.250g, and within 0.005 g of this value (2.0% error) . The liquid was filled to a height in the aquarium of approximately 61.0 ± 1.3 cm. The aquarium has side lengths of 48.0 ± 0.1 cm and 44.0 ± 0.1 cm, so the total volume of liquid would be 128.8 ± 2.8 L (2.2% error). The distance to the camera was measured to be 21.3 ± 0.5 cm (2.3% error). The angle was set for 55.0 ± 1.0° (1.8% error), through the use of a Thorlabs precision angle mount. Because the distance along the beam and the distance back to the camera from a point on the beam is determined from geometry with the distance between the laser and camera, as well as the incidence angle, the distances along the beam and back to the camera have an error of 4.14%. Plugging these values into equation 17 yields an error of 5.9%.

2.2 Equipment

2.2.1 Equipment Mounting & Set up

The experiment was first conducted with an approximately 2 metre long black PVC tube, filled with water. However, this system had issues with circulation and a large angle of

measurement for the laser (as will be further explained in section 2.2.c). To implement an improved circulation system and take images at a smaller angle, the experiment was then conducted in a 200 L aquarium. The aquarium was fitted with cardboard around the outside to minimize any stray light entering the system. The floor and walls of the aquarium were covered with a black foam material to stop any internal reflection of light from the glass.

The aquarium experiments were conducted with a mounting device constructed with aluminum extruded rail. The laser was mounted inside an optical tube, which was attached to a manual rotation mounting device. Attached on the other side of this is an optical tube connected to a 90° angle beam splitter. With the rotation mount, the angle of the beam was able to be more precisely set. The mounting device is shown in Figure 2.1 below. Figure 2.2 illustrates the geometry of the field of view of the camera (31.76° degrees, horizontal).

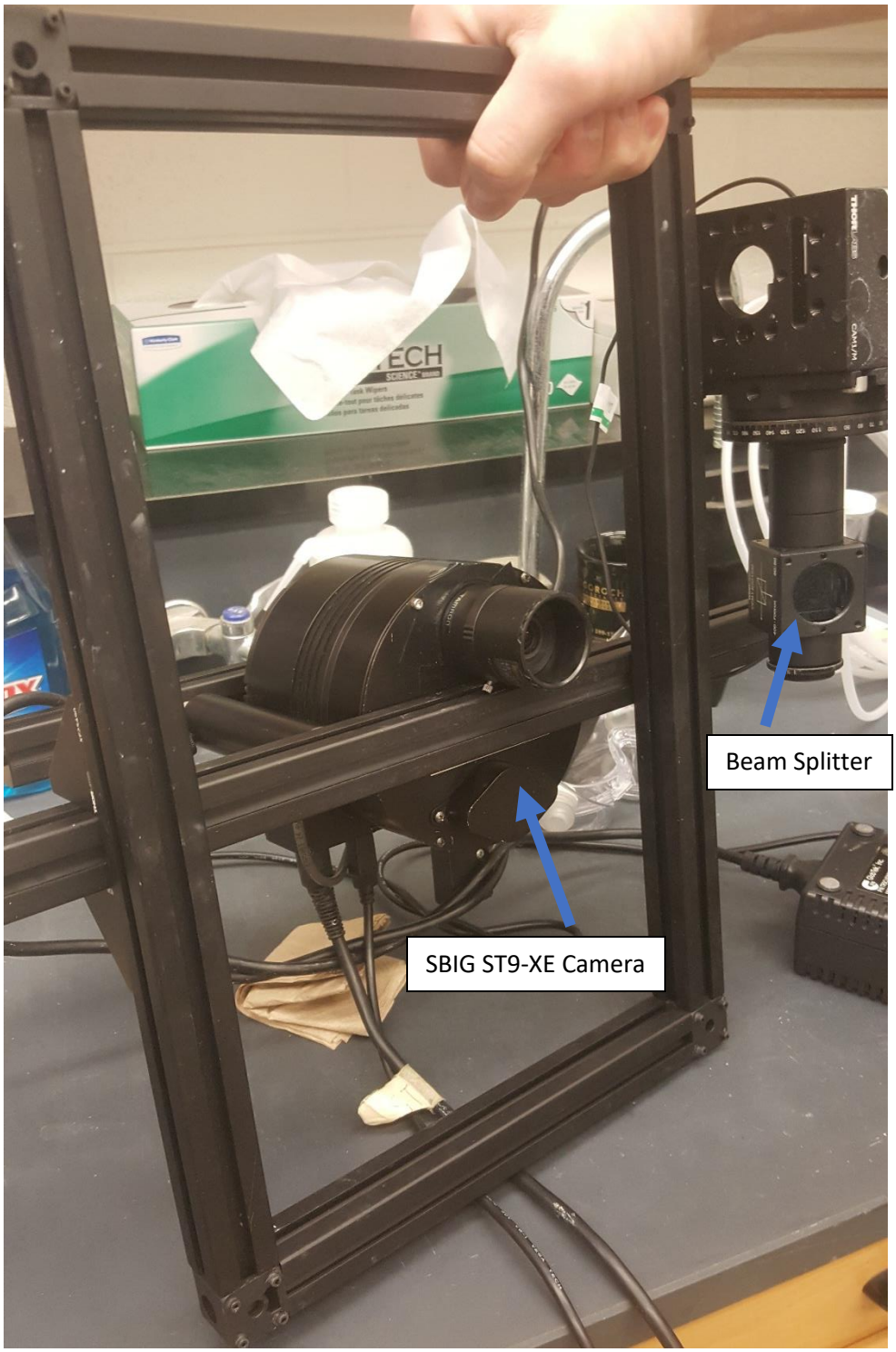

Figure 2.1 – Camera & Mount. *The part on the right side of the mount is the beam splitter and laser rig that holds the laser at the specified angle.*

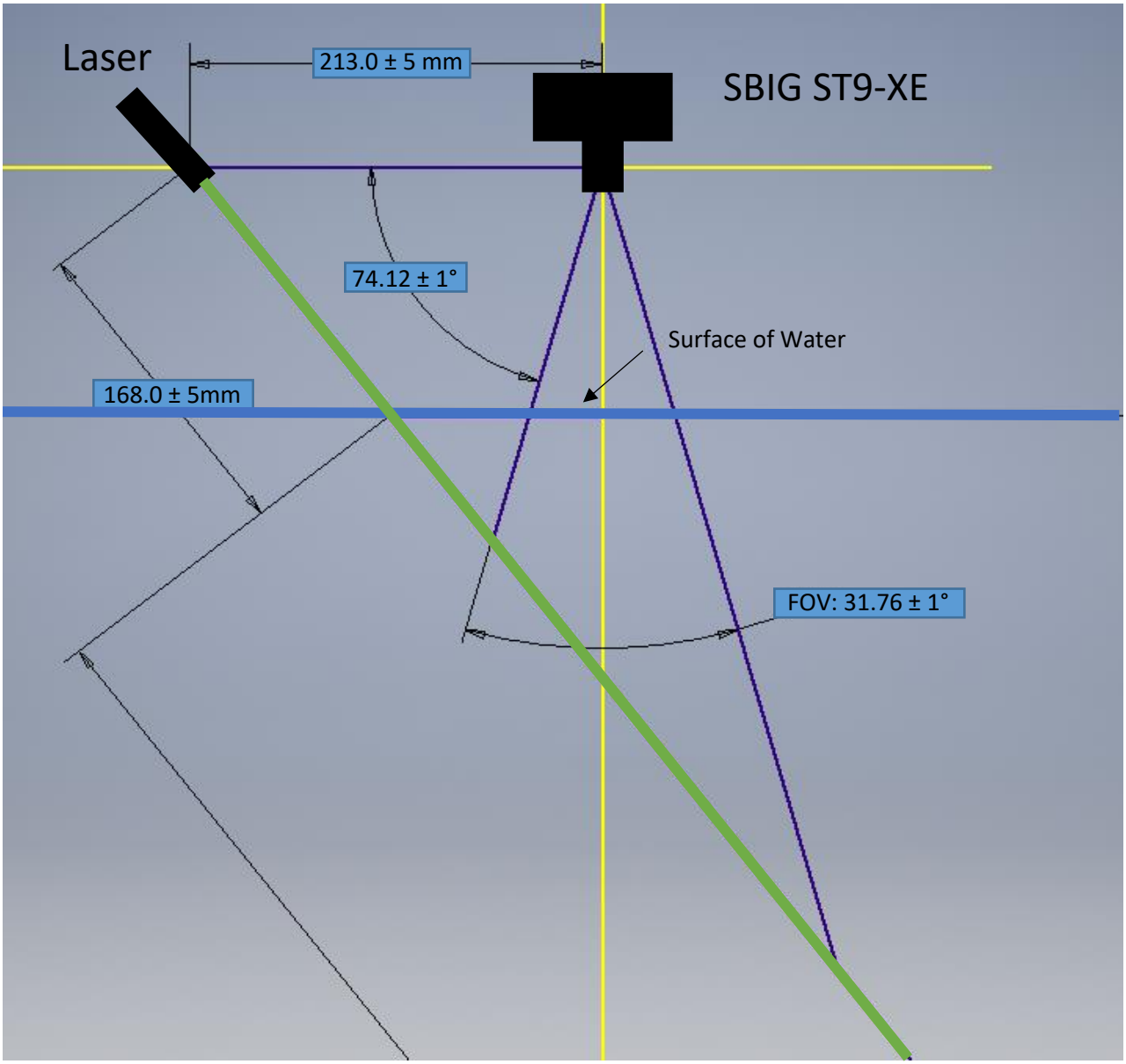

Figure 2.2 – Camera and Laser Geometry. *The green line represents the laser beam path (ignoring refraction). The blue horizontal line represents the surface of the water. The yellow lines represent the axes of the system, with the SBIG ST9-XE camera at the origin.*

2.2.2 Lasers

Initially, the lasers used were low powered (4.5 mW) battery-operated laser pointers, at wavelengths of approximately 450 nm (blue) and 550 nm (green). The lasers were aimed at an angle of approximately 2-3 degrees in relation to the axis of the length of the tube. Later, the

battery-powered laser pointers were replaced with laser diodes attached to a power supply. The battery-powered lasers experienced a decrease in the power output as the batteries were drained. This could lead to false positives when analyzing the images, as the amount of backscatter would appear to decrease faster than it was decreasing in reality. With a power supply, the laser diodes would not experience this decrease. Measuring the intensity of the light of the diodes over a period of time found negligible fluctuation. The diodes used were 4.5 mW, at wavelengths of 451.9 nm, 514.3 nm, and 638.0 nm.

2.2.3 Camera & Lens

The camera used for the duration of this study was an SBIG ST9-XE camera with a CFW8 color filter wheel, featuring red, blue, green, clear and lunar filters. The camera has a Kodak 512x512 pixel Enhanced KAF-0261E CCD, with each pixel having a size of 20x20 microns (Santa Barbara Instrumnet Group, 2005). The CCD has a Full Well capacity (the total number of electrons that can be captured in a single pixel) of 150,000 e- . The camera was first fitted with a Kenko 400mm F8 mirror lens with a manual focus. This camera is primarily used for astronomical research – it is very sensitive and can collect photons from very dim stars with a user-defined exposure time. This sensitivity makes such a camera an ideal choice for research where light dimming is to be measured.

The 400mm lens was found to only allow a small portion of the laser to be imaged. To increase the length of the laser imaged, the 400mm lens was replaced with a 4-12 mm manually variable CCTV lens, which allowed the camera to image a longer section of the laser at a larger incident angle. As there was a longer portion of laser available for analysis, there was also more data obtained from the laser.

2.2.4 Circulation

For the initial experiments in the PVC tube, a small 5 watt Hydor Koralia Evolution 550 Aquarium circulation pump was placed at the far end of the tube and powered on during the experiment. The pump was intended as a method to keep particles suspended throughout the tube, and prevent them from settling at the bottom. However, it was found that the Koralia pump being used was not sufficiently powerful enough to keep particles suspended and homogenized throughout the length of the tube. A new circulation system was devised, consisting of a more powerful Wayne PC2 230 watt transfer pump, attached to four hoses. The hoses were paired with a t-shape connector, then the paired hoses were attached to the inlet and outlet of the pump. This system allowed for improved circulation. However, particles were still found to be settling at the bottom of the system, so a procedural change was made to mitigate this issue (described in the "Procedures" section). Figure 2.2 illustrates the experimental set-up. Figure 2.3 is a picture of the set-up during an experiment.

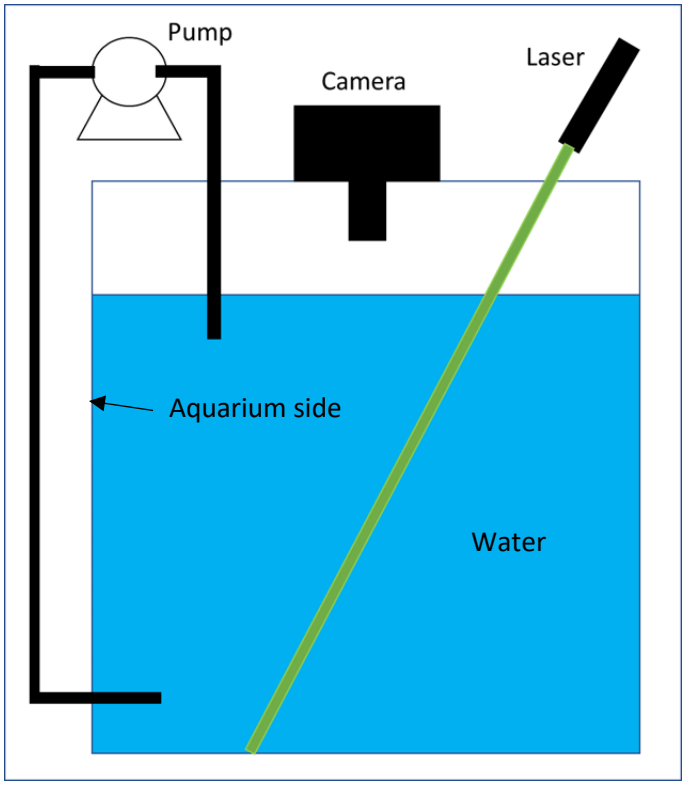

Figure 2.3 – Illustration of experimental set up. *Side view of set up*. *Green line represents laser path, ignoring refraction.*

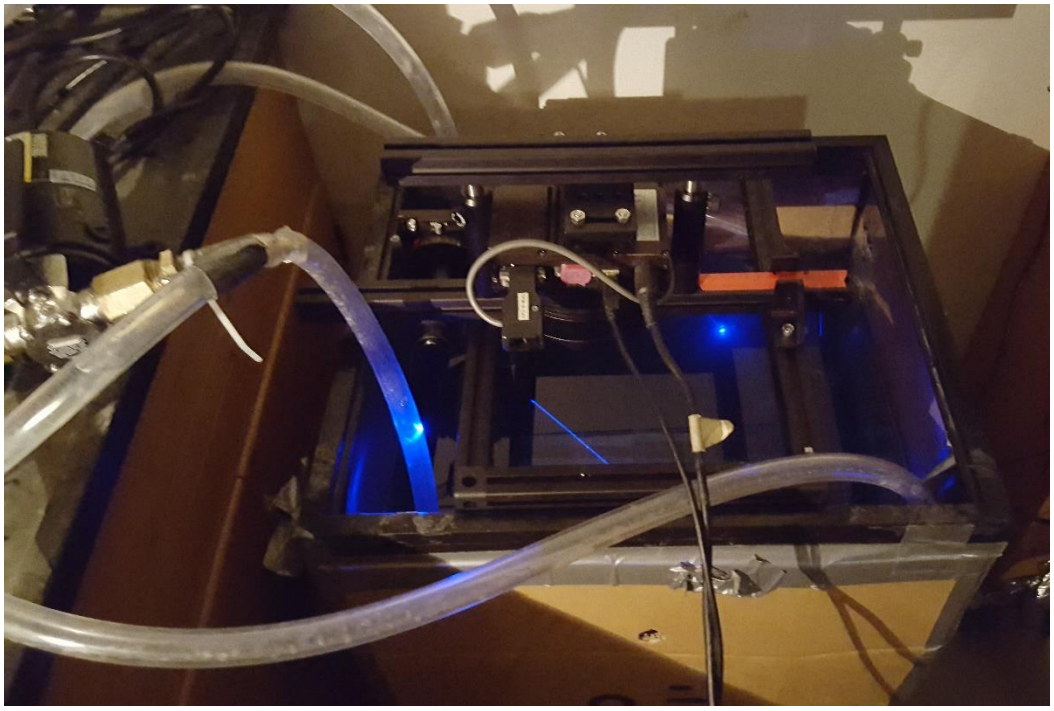

Figure 2.4 – Mounting device on top of aquarium. *The clear tubes are attached to the pump (left) and to each corner of the aquarium. The blue beam of the laser is visible in the aquarium. The orange tape strip visible had markings to denote the position of the camera*

2.2.5 Digital Scale

An Ohaus ScoutPro digital scale was used for measuring out a specified mass of the particles.

2.3 Controlled Parameters

Several parameters were controlled throughout this experiment. The following table summarizes these controls.

Parameter	Value	Method of Controlling/Measuring
External Light	Minimized	Experiment conducted in darkened room (no lights on – only light source was from a computer monitor a few feet away)
Particles in system	Increments of 0.250 ± 0.005g	Measured with Ohaus ScoutPro digital scale
Laser beam angle	55.0 ± 1.0° (before refraction)	360° Thorlabs Precision mount
Distance between laser and camera	210.0 ± 5.0 mm	Measured with measuring tape. Markings were used to align the camera position.
Camera CCD temperature	-20° below ambient	Controlled with CCDOps
Exposure Length	10 seconds	Controlled with CCDOps
Volume of liquid in aquarium	128.5 ± 2.7 L	Marking in tank to indicate where water should be filled to

Table 2.2 – Experimental Controls.

2.4 Materials

The initial experiments were conducted with silicon dioxide (SiO_2) particles. These particles have a diameter of approximately 2.0 microns. Because the distribution in diameter was

unspecified by the supplier, a sample of the SiO_2 particles was analyzed under a microscope to find the standard deviation of particle diameters. In order to reduce moisture in the particle samples and separate them, the particle samples were baked for several days at 95 °C and deionized. The standard deviation for the SiO_2 particles was found to be 0.2 microns. To examine the effect of varying the scattering material, titanium dioxide (TiO_2) particles were also used. These have a diameter range of 1.0-2.0 microns. As with the SiO_2 particles, the TiO_2 particles were examined under a microscope, and images were taken. The images were then analyzed with ImageJ to find the distribution of particles, shown below in Figure 2.3. Figure 2.4 is an example of one of the images that was analyzed.

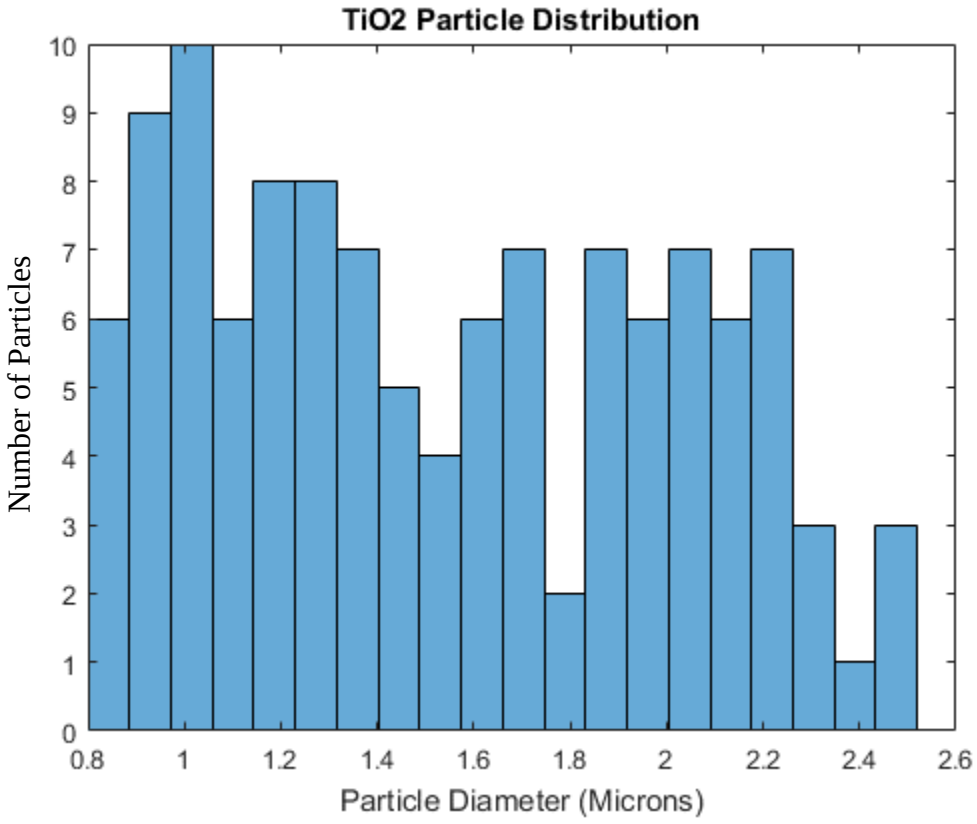

Figure 2.5 – Particle Distribution of TiO2.

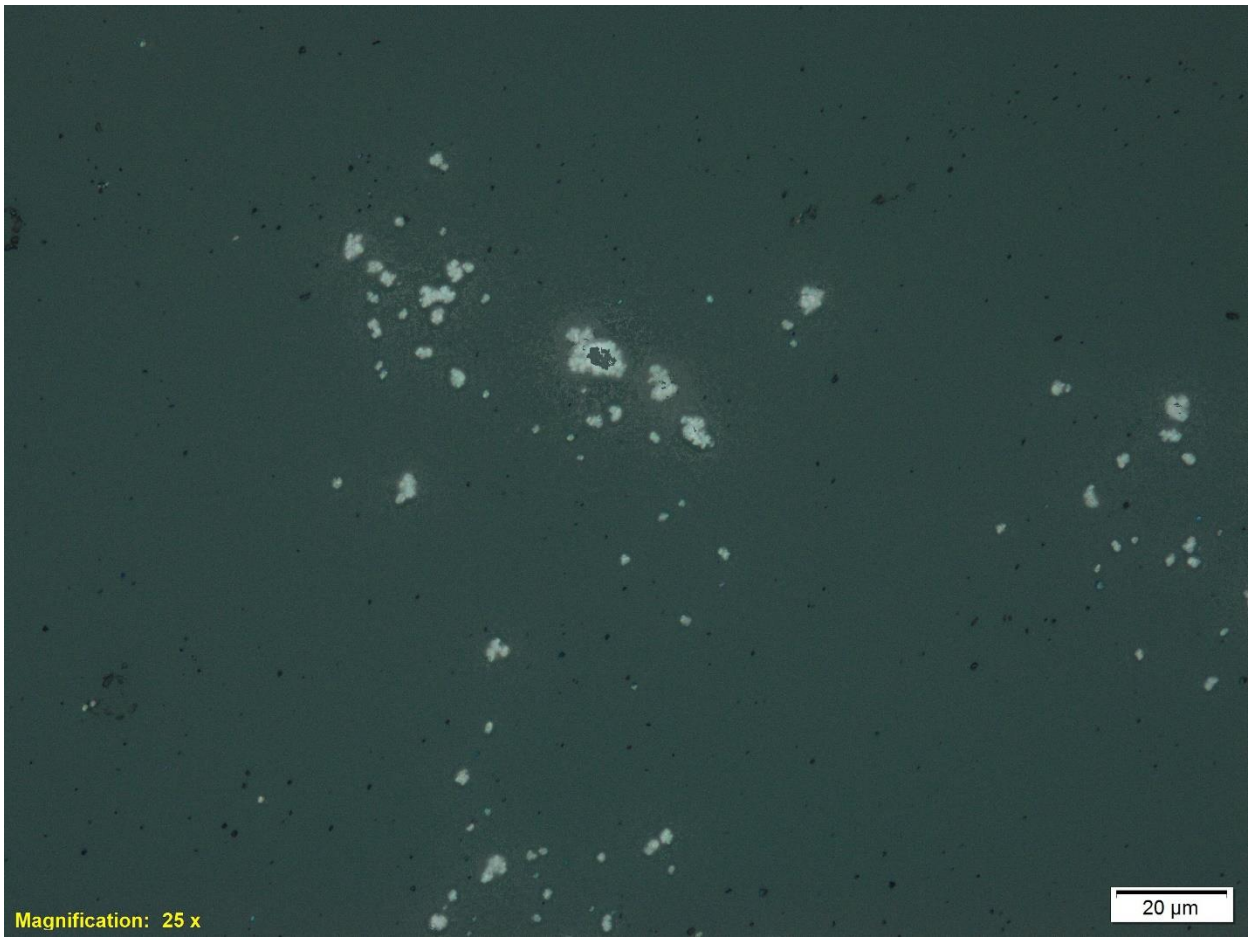

Figure 2.6 – Image of TiO_2 particles under microscope. *25x magnification.*

2.5 Procedures

The experiment is conducted in a dark environment, to minimize the amount of external light being picked up by the CCD on the camera. The experiment begins by taking a series of five flat field images (images where the camera is looking at a bright, evenly lit surface, such as the $BaSO_4$ integrating sphere pictured in in Figure 2.5) and five dark field images (dark images where the CCD takes a picture while the shutter is closed).

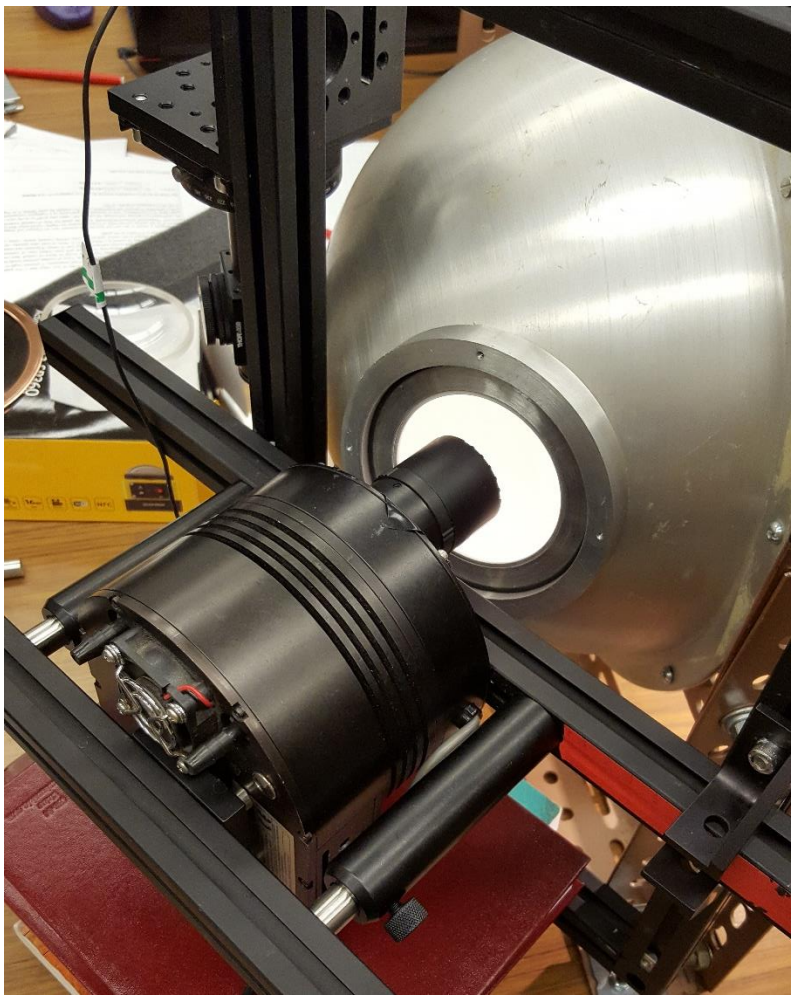

Figure 2.7 – Camera on aluminum mount taking flat field images. *The camera, with the 4-12 mm lens, is pointed inside of an integrating sphere, an apparatus that evenly distributes light on its surfaces.*

Once these images are obtained, images of the laser in water are taken with no particles added. Five is set as the standard number of images obtained for each set to optimize the amount of data being collected while minimizing the time required to perform the experiment.

Images were captured using CCDOps, a software that allows the user to control aspects of imaging with the CCD – for example, setting the exposure time. Prior to image capture, the cooling system of the camera was set to cool the CCD to approximately 20°C below ambient temperatures – usually between -5 to -10°C. Cooling the CCD minimizes any thermal noise that the CCD may

obtain. Once the camera's CCD reached the set cooling point (or reached the lowest possible point), flat field images and dark field images were captured, using the filter corresponding with the wavelength of the laser used for the experiment. Flat field images were taken so that the maximum pixel value was between 28,000 to 35,000 counts. Dark field images were taken to match the exposure time that is used during the experiment.

A series of five images are taken of the system. Taking multiple images is necessary so that if there are any anomalies in one image (for example, if a bubble formed and disrupted the laser beam), there are several others available for analysis. Once these images are taken, 0.25 ± 0.005 g of SiO_2 is added into the system and allowed to circulate and homogenize for approximately 1 minute. Another five images are taken. This process continues until the majority of the laser is no longer visible. Initial experiments had the camera taking pictures with an exposure time of one second or less. However, it was found that these images were yielding low quality results with a low signal-to-noise ratio, so the exposure time was later lengthened to ten seconds. This yielded clearer images with a higher signal-to-noise ratio, and ultimately better results, as will be further detailed in the analysis section.

Particles were found to be settling at the bottom of the aquarium, rather than mixing homogenously in the system. This was corrected by adding a new step to the experimental procedure. Instead of adding particles directly to the system, a small amount of the water in the aquarium was removed with a beaker. The particles would then be added to that, then mixed well until no more particles were visible at the bottom of the beaker and the liquid was homogenously mixed. This water would then be added back into the system, keeping the amount of water in the system constant. Figure 2.6 shows the digital scale with the beaker.

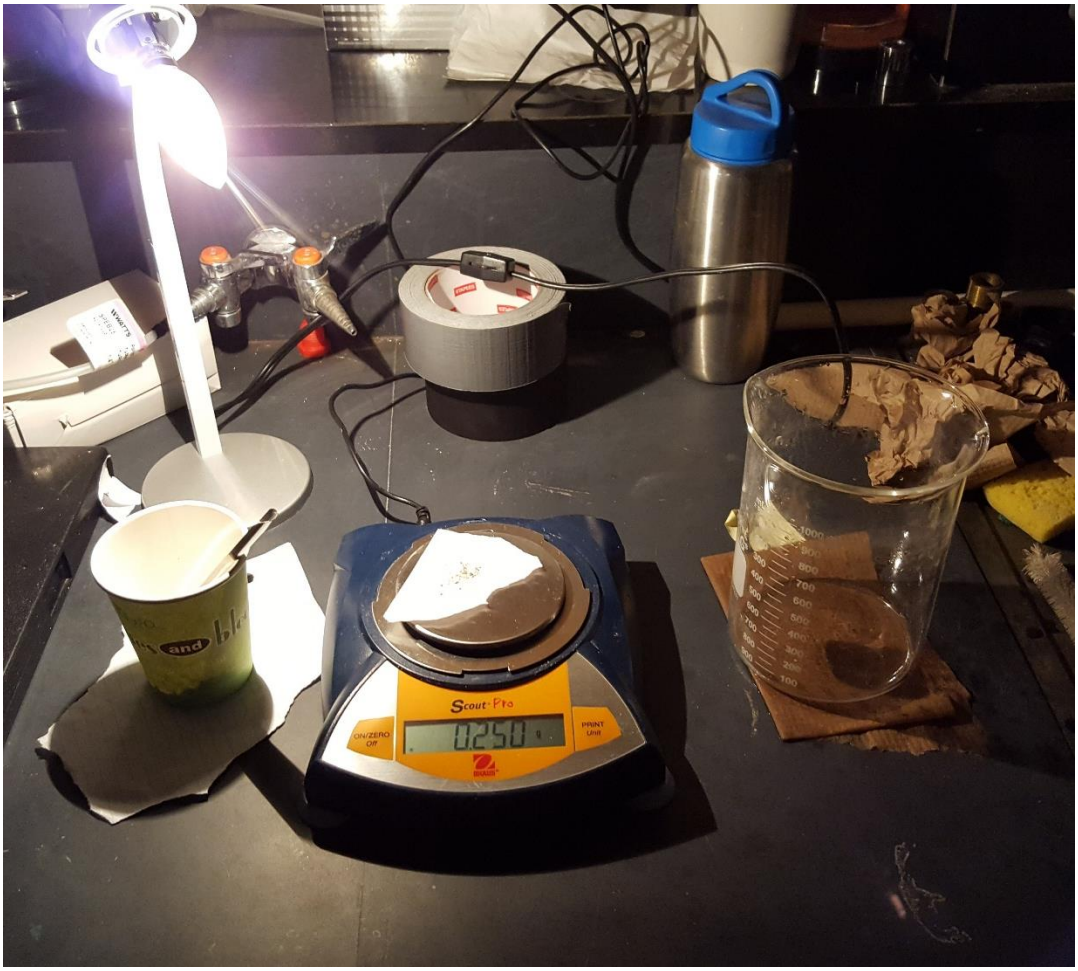

Figure 2.8 – SiO_2 particles measured on digital scale. *The beaker at the right would be used to remove water from the aquarium, and the particles would be added to the beaker and stirred. Once the particles were well mixed, the mixture would be added back into the system.*

Multiple experiments were conducted to determine what the best angle for the laser would be. It was found that 55° was optimal for experiments conducted in the aquarium (before accounting for refraction after the laser enters the water), as it allowed for a significant portion of the laser to be imaged, while also allowing for greater exclusion of the initial and termination points in the image (that is, the points of light corresponding with where the laser is at the water's surface, and where the laser beam terminates at the bottom of the aquarium). These points were very bright, and often caused over saturation of the CCD, resulting in lower quality data (seen in

Figure 2.7). Therefore, images were taken to exclude these points. The mounting device had the camera attached to a sliding bar that could allow for the camera to be position such that these points were excluded.

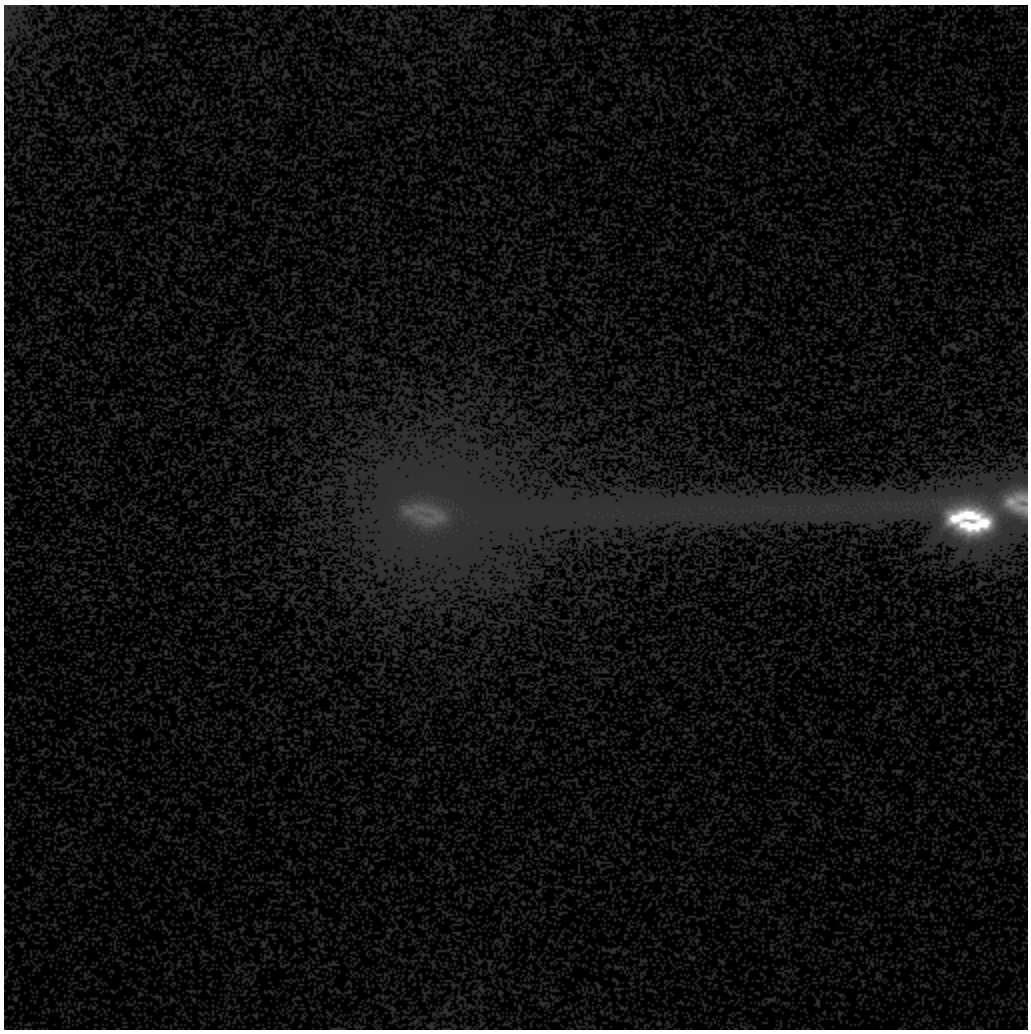

Figure 2.9 – Example of image with oversaturation of starting and terminations points. *In this image, the actual beam is barely visible.*

The experiment was also conducted with TiO_2 and multiple laser wavelengths. The experiments were also repeated several times to obtain larger data sets. Figure 2.4 is an illustration of the final experiment configuration.

3. Analysis of Images & Data

After the images are obtained, they are analyzed in MATLAB. First, the images are corrected with the flat-field and dark field images taken prior to the experiment. This correction is applied as

$$corrected\ image = \frac{data - dark\ field\ average}{flat\ field\ average - dark\ field\ average} \tag{18}$$

The dark field images accounts for thermal noise on the CCD itself, while flat-field images correct for artefacts and anomalies due to the presence of dust, scratches or other potential sources of error on the filter or camera lens.

After this correction, a background subtraction is done, where the average value of a square area located away from the laser beam is subtracted from the data analyzed. This accounts for any variation in background lighting which would otherwise brighten the laser and skew the results. Once the background subtraction is done, the image is analyzed. The laser in the image is divided into rows of pixels. These rows are then averaged together to form a single vector of data. A box-car average smoothing is then applied. With this smoothing method, a data point is averaged with the previous and subsequent data points, and then that value is reassigned to a new array. This is illustrated in Figure 3.1.

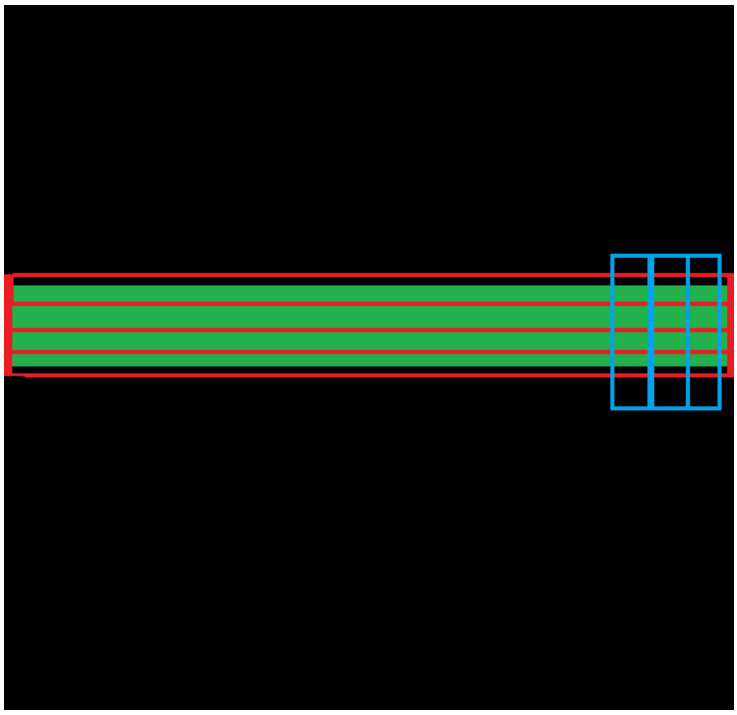

Figure 3.1 - Simplified representation of analysis. *Green represents the laser. The rows of pixels (denoted by red rectangles) are averaged together. The three columns of pixels from this laser are averaged together for smoothing (represented by blue rectangles).*

This is applied to every image taken. From this data, we can obtain the extinction coefficient (the value accounting for how light dims as it passes through a medium, in this case, the particle being added). The average extinction coefficient is found for each image series (i.e. the images taken at each level of number concentration in the aquarium) by fitting the data obtained from the laser to the Beer-Lambert Law. These averages were plotted, and a best fit for the data was found to determine the relation between the particle density and the turbidity of the system.

Averages are taken for each laser wavelength. As it was discovered that two different angles may have been inadvertently used in the data gathering process (discussed further in chapter 5), with earlier experiments being conducted at an incident angle of 55 degrees and more recent

experiments conducted at an incident angle of 35 degrees, the extinction values were separated by incidence angle as well as wavelength.

The Bessel functions and efficiency factors were calculated using the Mie Scattering Calculator by Scott Prahl (Prahl, 2018). Using this calculator and refractive index values, efficiency factors for TiO_2 and SiO_2 were found. For TiO_2, since the powder consists of particles over a range of different radii, the efficiency factors were calculated for several different radii within that range. These values are listed in Table 6.1:

Particle Radius (microns)	**Q factor**	**Blue (451.9 nm)**	**Green (514.3 nm)**	**Red (638.0 nm)**
r = 0.250	Qext	2.156	3.428	1.278
	Qsca	2.156	3.428	1.278
	Qback	3.116	1.290	9.044
r = 0.500	**Q_{ext}**	**2.284**	**2.268**	**2.346**
	Q_{sca}	**2.284**	**2.268**	**2.346**
	Q_{back}	**4.198**	**0.361**	**11.175**
r= 0.750	**Q_{ext}**	**2.131**	**2.539**	**2.775**
	Q_{sca}	**2.131**	**2.539**	**2.775**
	Q_{back}	**13.899**	**14.036**	**15.972**
r=1.000	**Q_{ext}**	**2.080**	**2.428**	**2.570**
	Q_{sca}	**2.080**	**2.428**	**2.570**
	Q_{back}	**0.697**	**1.770**	**10.227**

Table 3.1 - Q factors for TiO_2 at each wavelength

The bolded values represent values that are used in the experiment. However, in the analysis of the obtained data, the TiO_2 particles were assumed to have an average diameter of 1.5 microns, for simplicity. For the SiO_2 particles, the powder is given at a single diameter, but the efficiency factors are listed at multiple radii for comparison.

Particle Radius (microns)	Q Factor	Blue (451.9 nm)	Green (514.3 nm)	Red (638.0 nm)
r = 0.250	Qext	0.425	0.305	0.175
	Qsca	0.425	0.305	0.175
	Qback	0.006	0.015	0.005
r= 0.500	Qext	1.567	1.192	0.744
	Qsca	1.567	1.192	0.744
	Qback	0.003	0.001	0.002
r=0.750	Qext	2.765	2.269	1.542
	Qsca	2.765	2.269	1.542
	Qback	0.009	0.007	0.0128
r=1.000	**Q_{ext}**	**3.415**	**3.116**	**2.368**
	Q_{sca}	**3.415**	**3.116**	**2.368**
	Q_{back}	**0.048**	**0.015**	**0.004**

Table 3.2 - Q Factors for SiO_2 at each wavelength

In this experiment, N (the number of particles per unit volume) is calculated by dividing the total mass of particles added to the system by the mass of a single particle (based on the radius and particle density).

4. Results of Image Analysis & Discussion

The images of the beam were analyzed for each image. From the images themselves, the "shrinking" of the laser (i.e. the reduction of the amount of the laser that is visible) was very apparent. This can be seen in the image series in Figure 4.1:

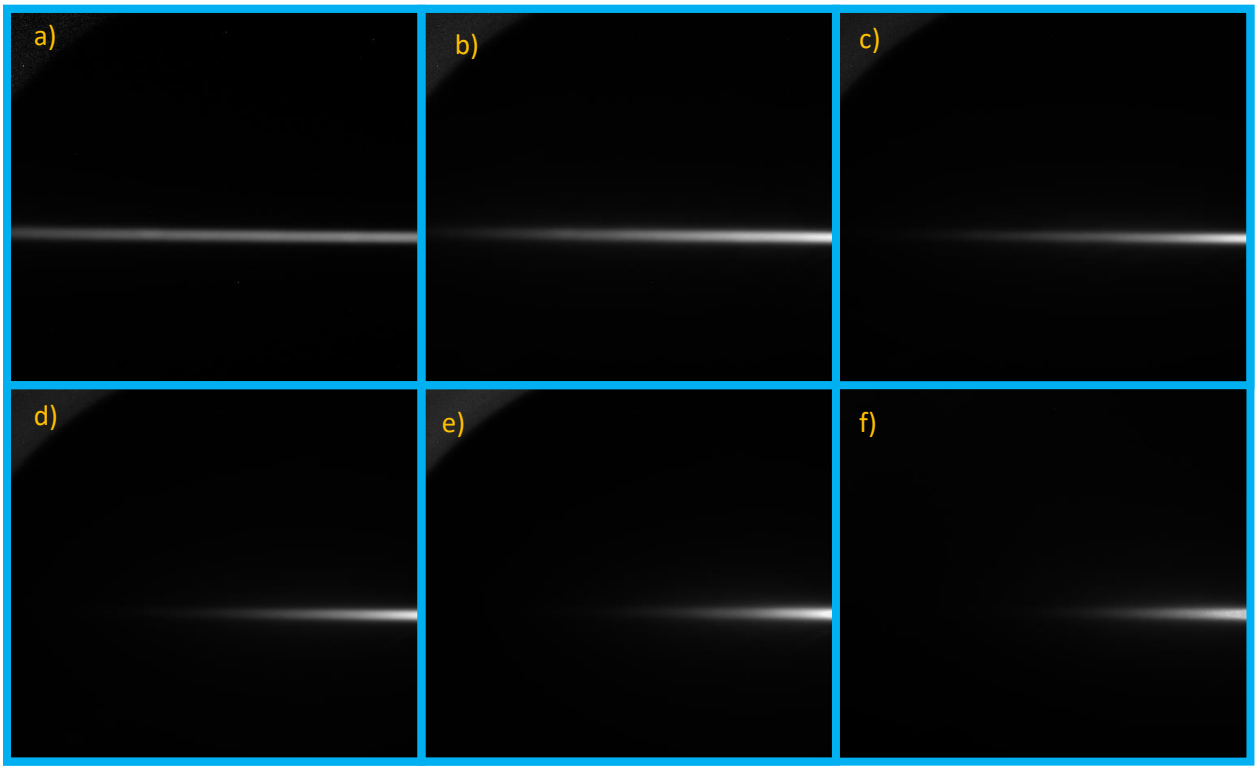

Figure 4.1 – Sample images of laser. *Taken from Trial 52 with green laser, at a) 0.250g TiO2 added, b) 1.250g, c) 2.250g, d) 3.250g, e) 4.250g, f) 5.250g*

For each wavelength and particle type, it was noted that at low particle values, the modeling equation (based on the Beer Lambert Law as previously noted) was a very poor fit, but the fit improved greatly as the number density of the system increased. This can be seen in Figure 4.2. In this figure, red lines represent the data and blue lines represent the modeling curve, according to the Beer-Lambert Law. In these graphs, the standard deviations were found to be

0.079 for 0 g of added particles, 0.310 for 1 g of added particles, 0.280 for 3 g of added particles, and 0.252 for 5 g of added particles. The error, calculated from equation 15, was found to be 0.064 – within one standard deviation for each graph.

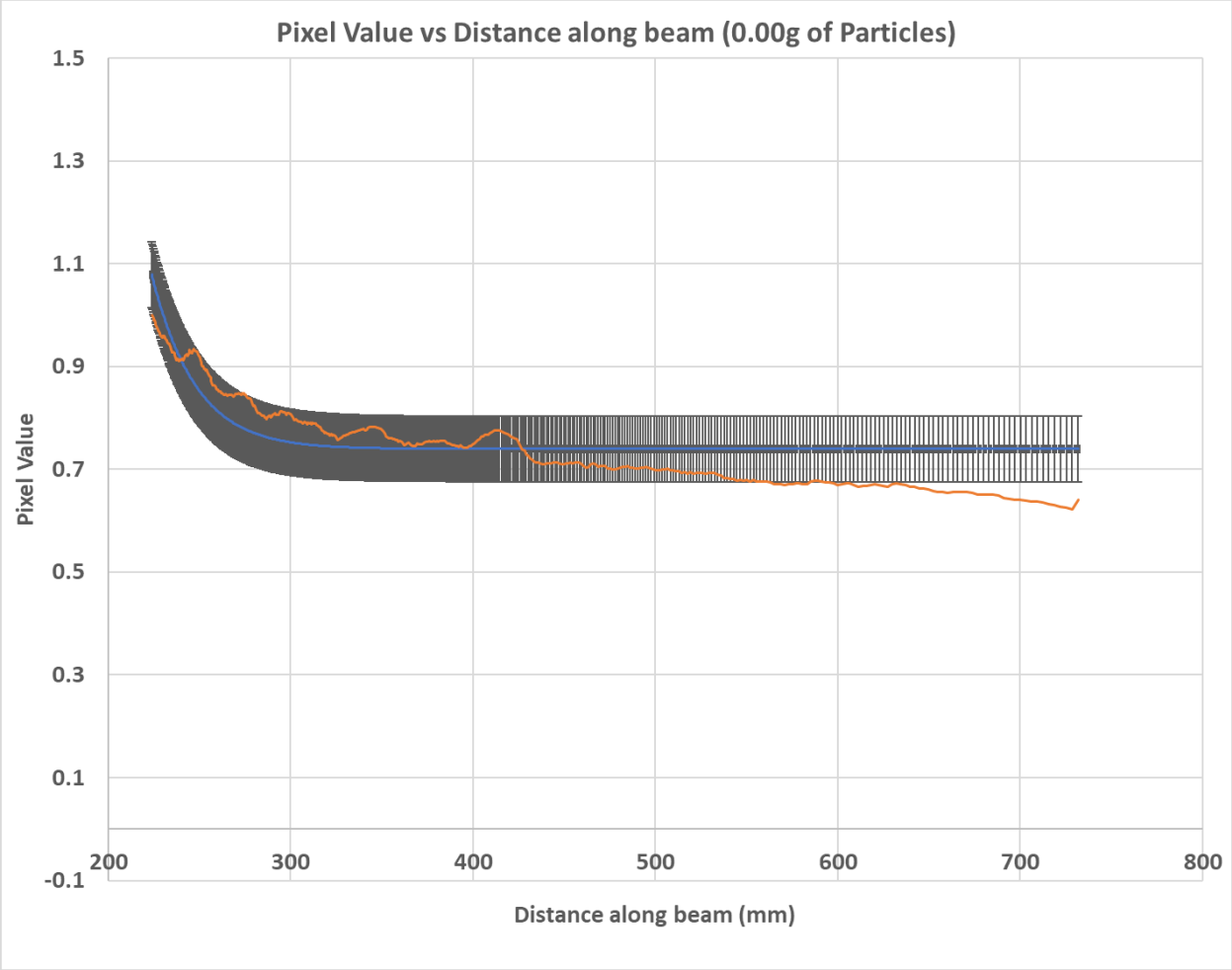

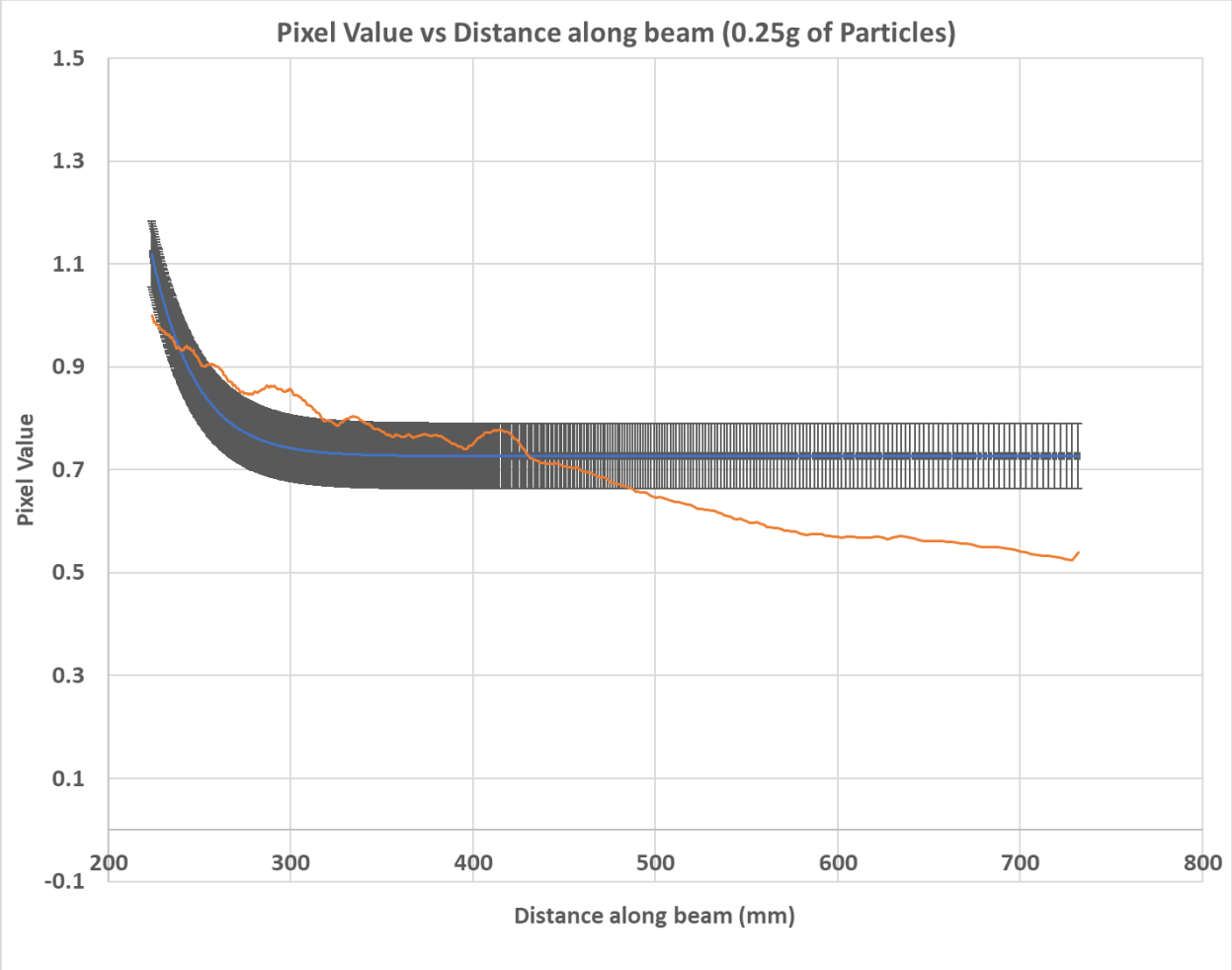
Pixel Value vs Distance along beam (0.25g of Particles)
1.5
1.3
1.1
0.9
0.7
0.5
0.3
0.1
-0.1
Pixel Value
200
300
400
500
600
700
800
Distance along beam (mm)

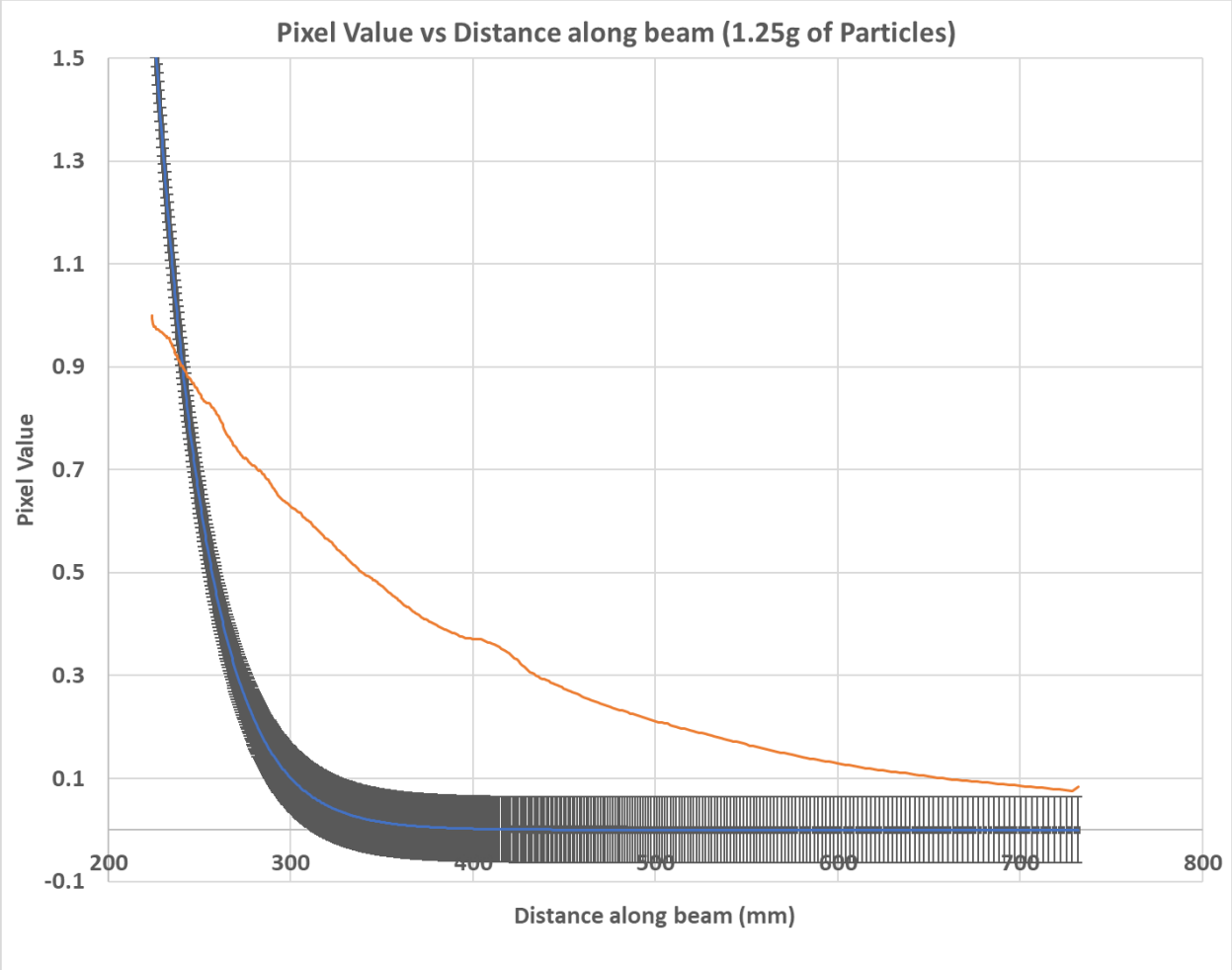
Pixel Value vs Distance along beam (1.25g of Particles)
1.5
1.3
1.1
0.9
0.7
0.5
0.3
0.1
-0.1
Pixel Value
200
300
400
500
600
700
800
Distance along beam (mm)

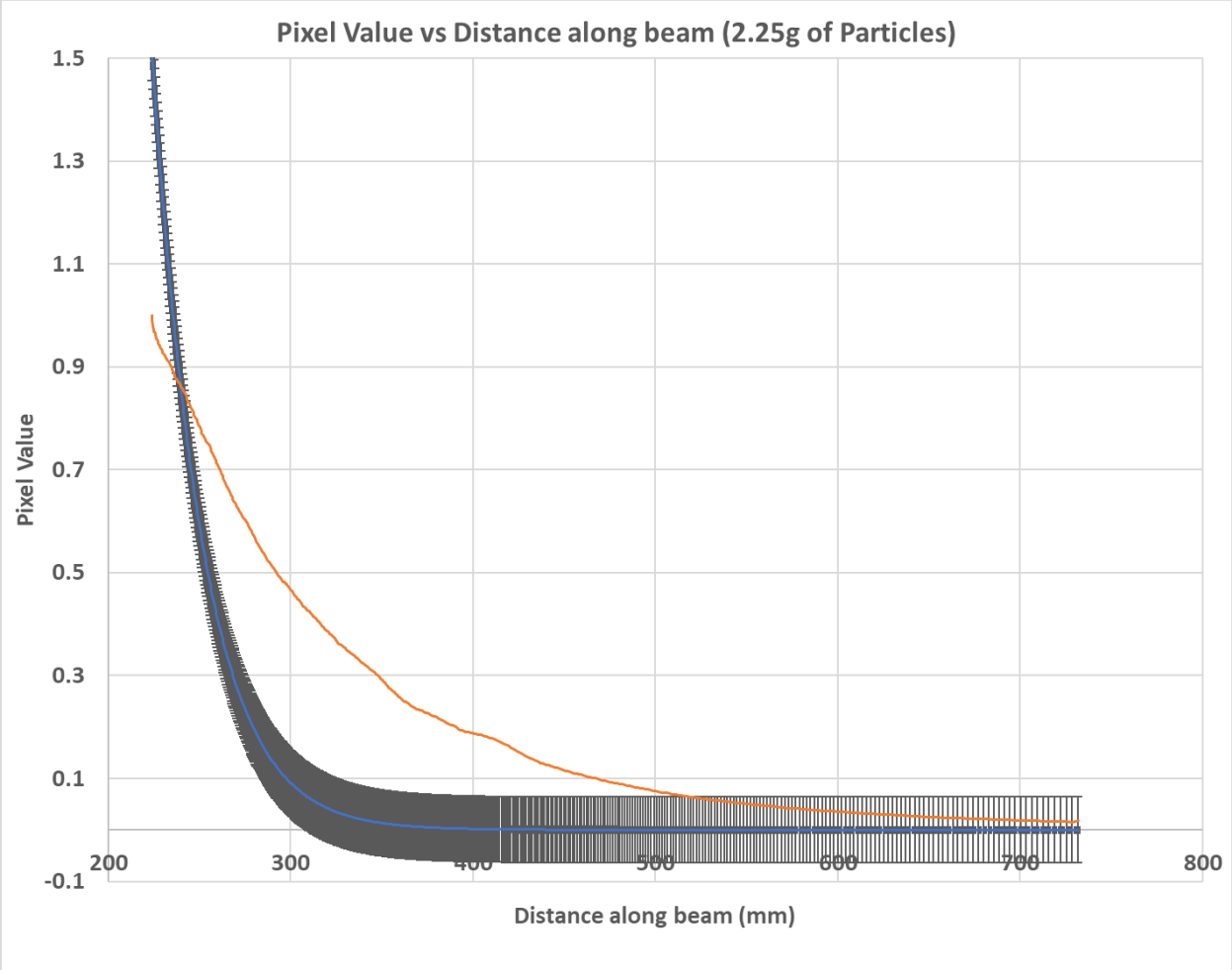
Pixel Value vs Distance along beam (2.25g of Particles)
Pixel Value
1.5
1.3
1.1
0.9
0.7
0.5
0.3
0.1
-0.1
200
300
400
500
600
700
800
Distance along beam (mm)

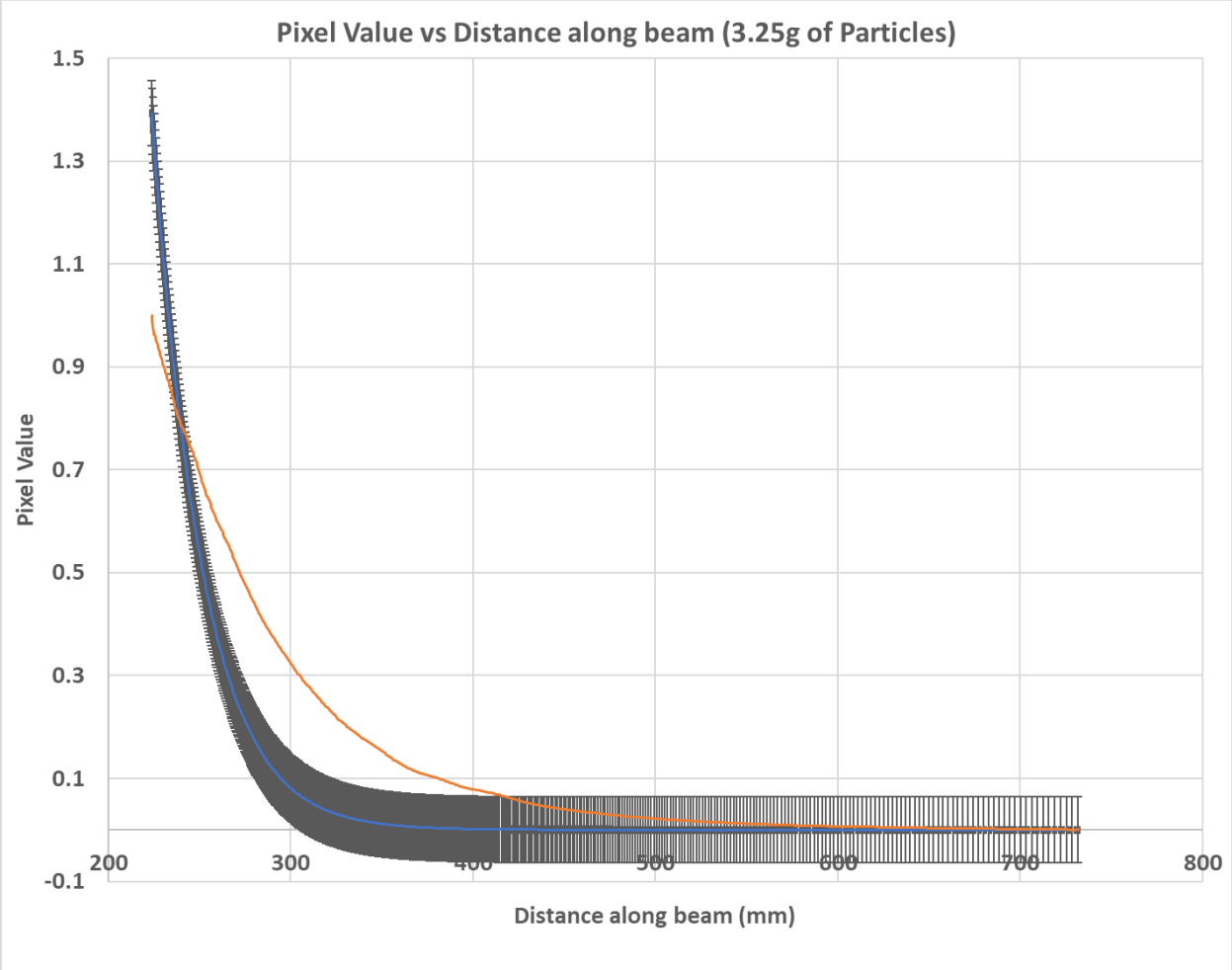
Pixel Value vs Distance along beam (3.25g of Particles)
1.5
1.3
1.1
0.9
0.7
0.5
0.3
0.1
-0.1
Pixel Value
200
300
400
500
600
700
800
Distance along beam (mm)

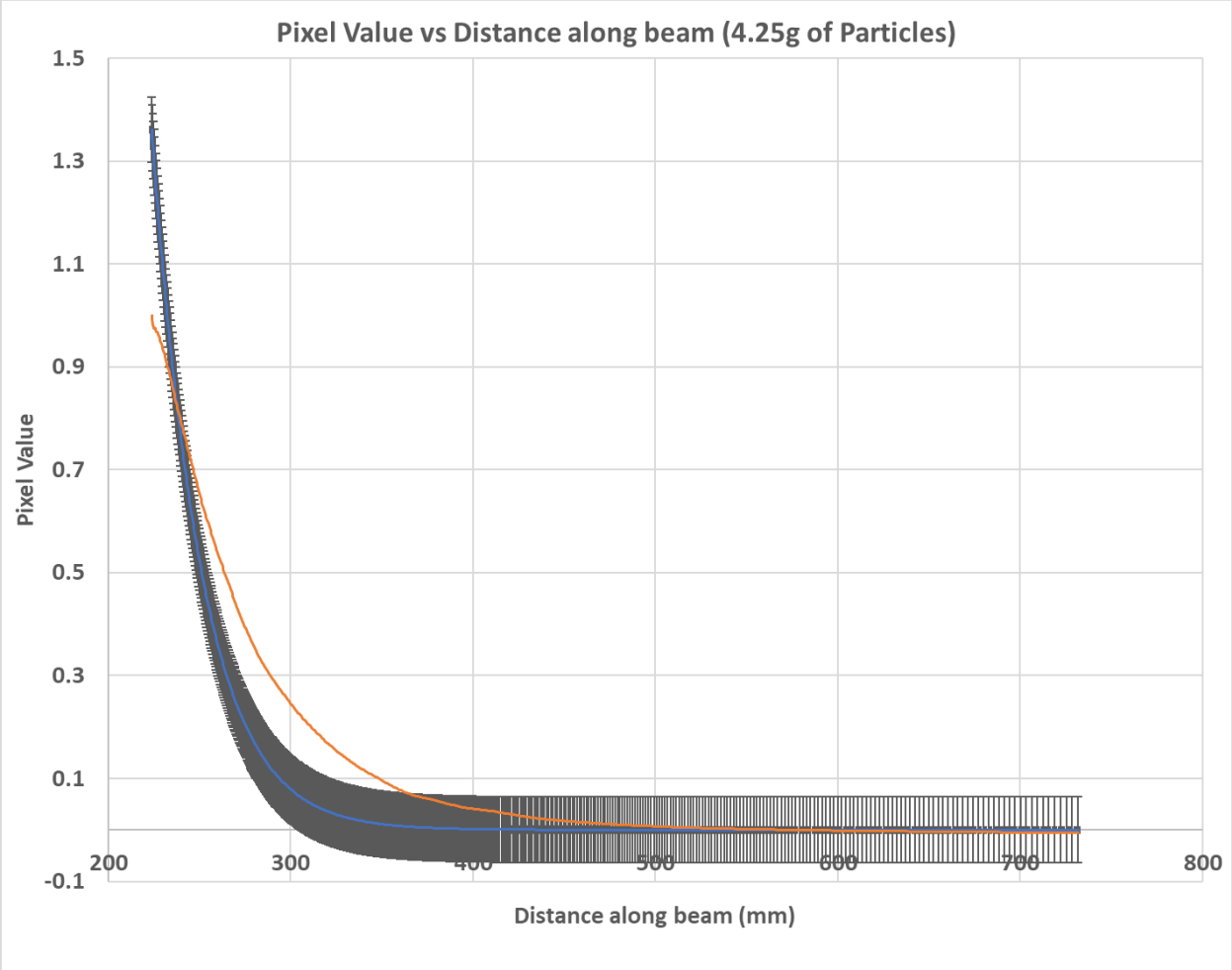
Pixel Value vs Distance along beam (4.25g of Particles)
1.5
1.3
1.1
0.9
0.7
0.5
0.3
0.1
-0.1
Pixel Value
200
300
400
500
600
700
800
Distance along beam (mm)

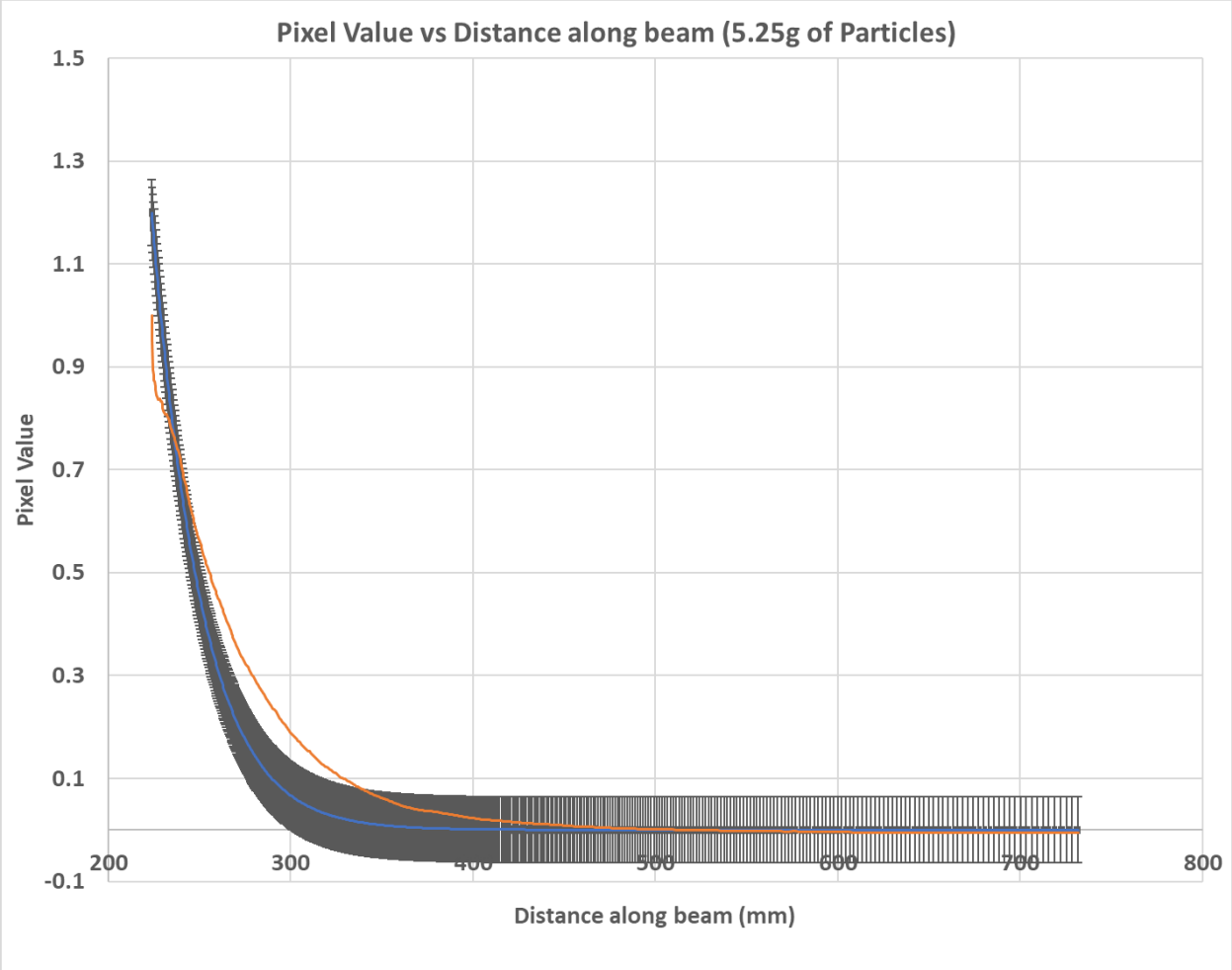

Figure 4.2 – Pixel Value vs Distance. *These graphs are from Trial 52, which utilized the green wavelength laser with TiO_2 particles.*

When this analysis was done for all images, the extinction coefficient for each set was plotted. The results for TiO_2 particles are show below:

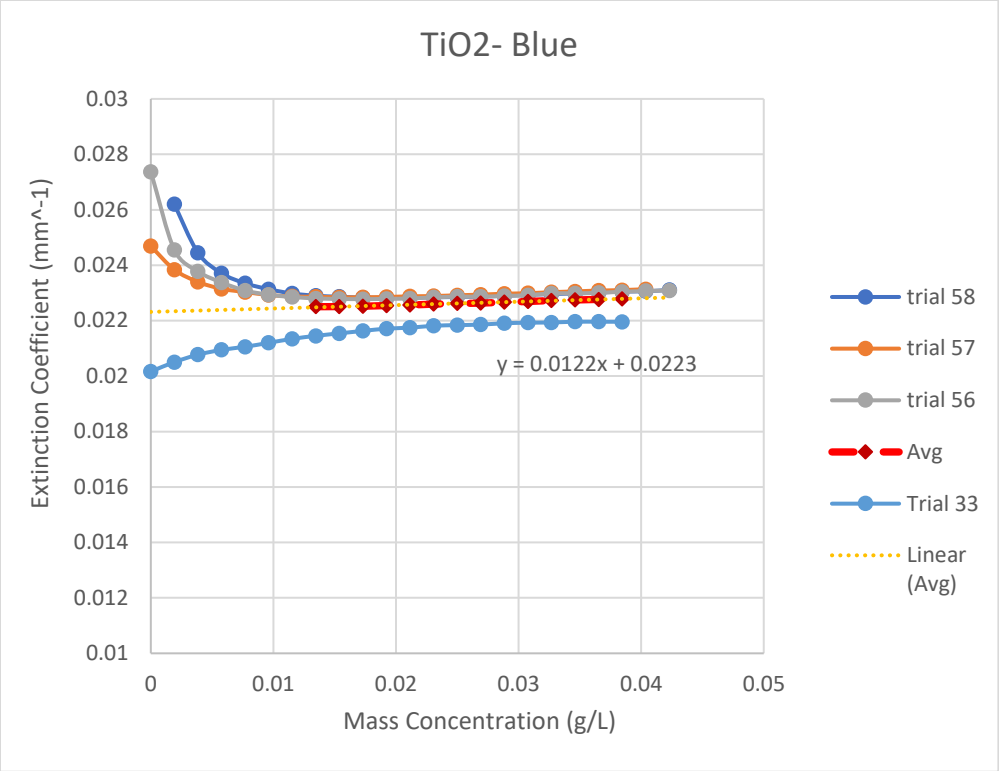

Figure 4.3 - TiO_2 particles at blue wavelength.

In Figure 4.3 above, the results from four trials are shown. Trials 56, 57 and 58 are closely grouped together. Trial 33 is positioned lower than the others, and always increases, whereas the slopes from Trials 56-57 first experience a sharp negative slope, before changing to a positive slope. An average of this data is plotted in red with a linear trendline (data for the decreasing values are ignored, and only positively sloped data is shown). Sources of the difference between Trial 33 from the others are discussed in chapter 5. Each data point of Trial 33 was found to be greater than 1.00 standard deviation and less than 2.00 standard deviations from the average.

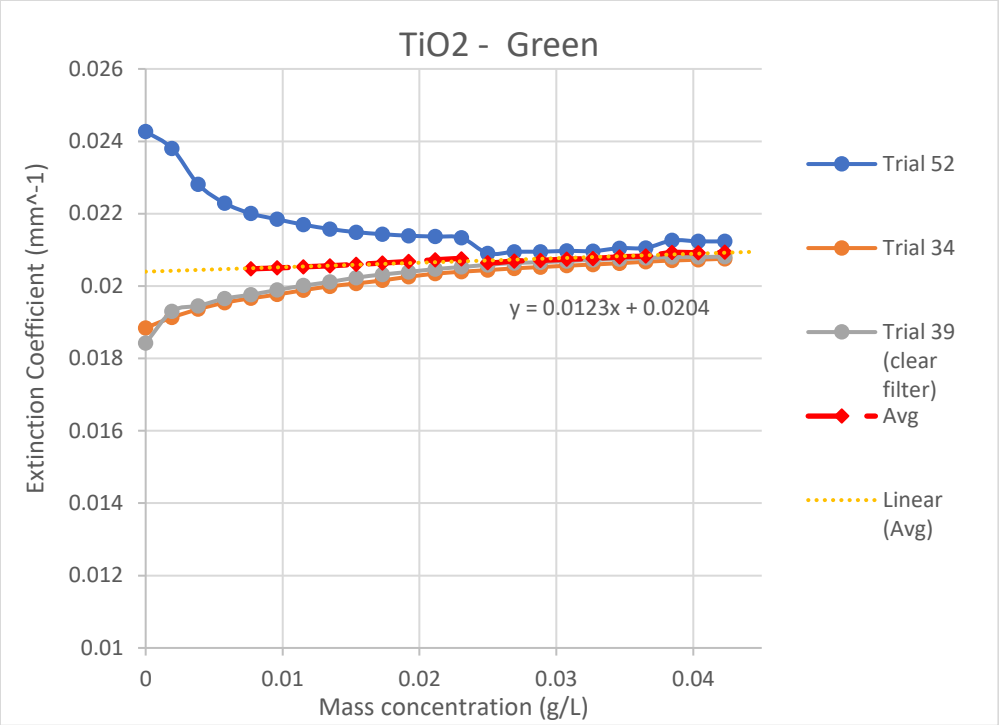

Figure 4.4 – TiO_2 particles at green wavelength.

In the above plot, we can see that Trials 34 and 39 produced similar results, and Trial 52 produced a curve that initially starts at a high value, decreases, and begins to increase again, similar to Trials 56-57 in the previous plot. The average is plotted in red. It should also be noted that Trial 39 was conducted using the clear filter, rather than the green filter. From the above data, it appears that this did not have a significant impact on the output results. Each data point for Trial 52 was found to be between 1.00 and 1.50 standard deviations from the average.

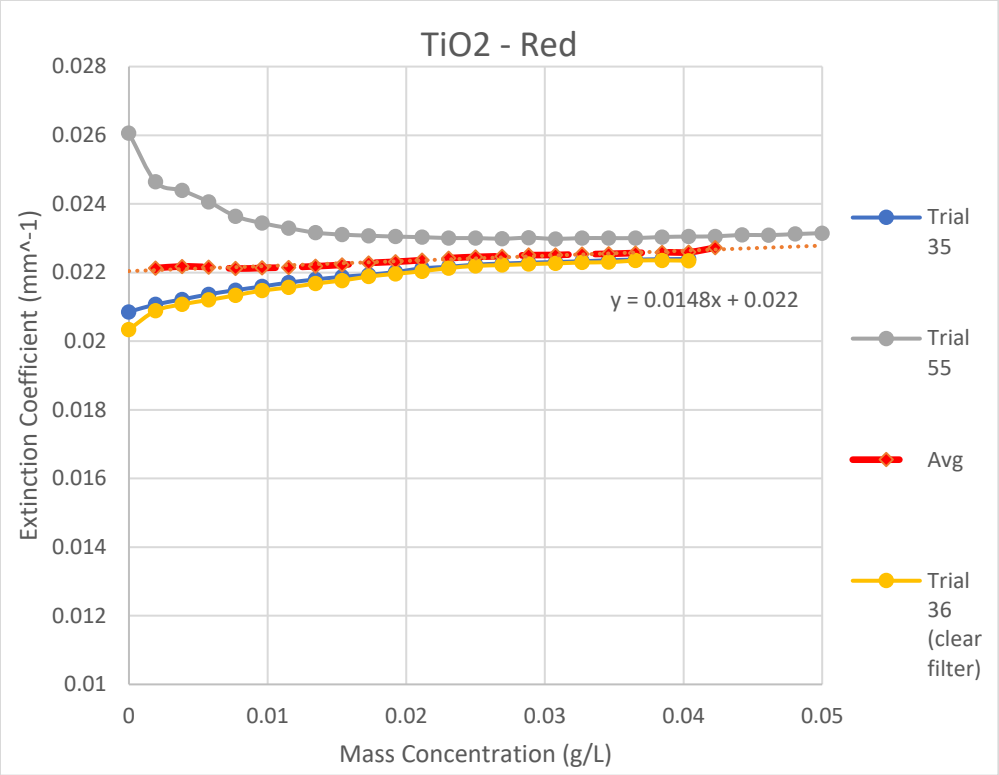

Figure 4.5 – TiO_2 at red wavelength.

In Figure 4.5, the outlier is again apparent in the data for Trials with the red wavelength laser. Trials 35 and 36 are grouped closely together, while Trial 55 is positioned higher with the initially high value. Trial 36 was also conducted with a clear filter instead of the red filter, but seems to not produce a significantly different result. Each data point of Trial 55 was approximately 1.41 standard deviations from the average.

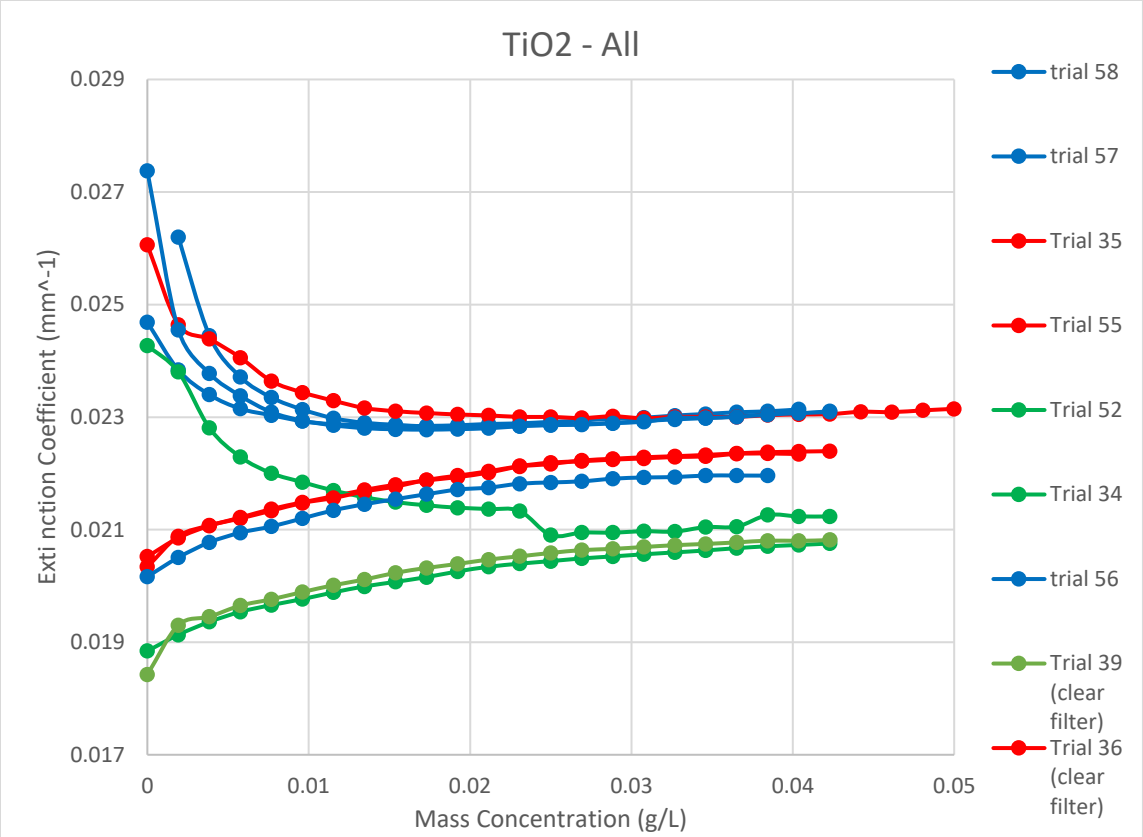

Figure 4.6 – Extinction Coefficients vs mass concentrations for TiO_2 particles at all wavelengths. *The color of each curve corresponds to the wavelength used for that trial.*

Figure 4.6 shows the data from all plots, where the color corresponds to the wavelength for that Trial.

The same plots were made for the SiO_2 particles:

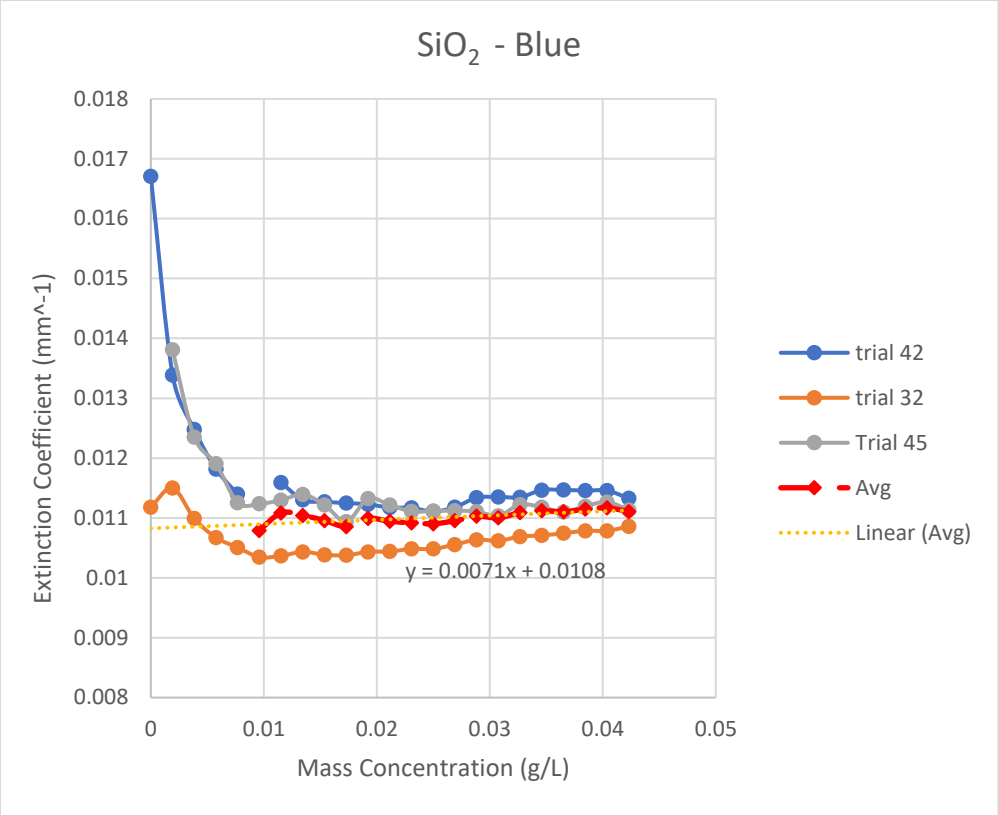

Figure 4.7 – SiO_2 at Blue wavelengths.

Figure 4.7 shows data from SiO_2 at blue wavelengths. The data appears to be grouped fairly close together with no outliers. However, the data also appears to experience greater deviation than what was seen with the TiO_2 data – the curves are not as smooth for SiO_2. The average is shown in red.

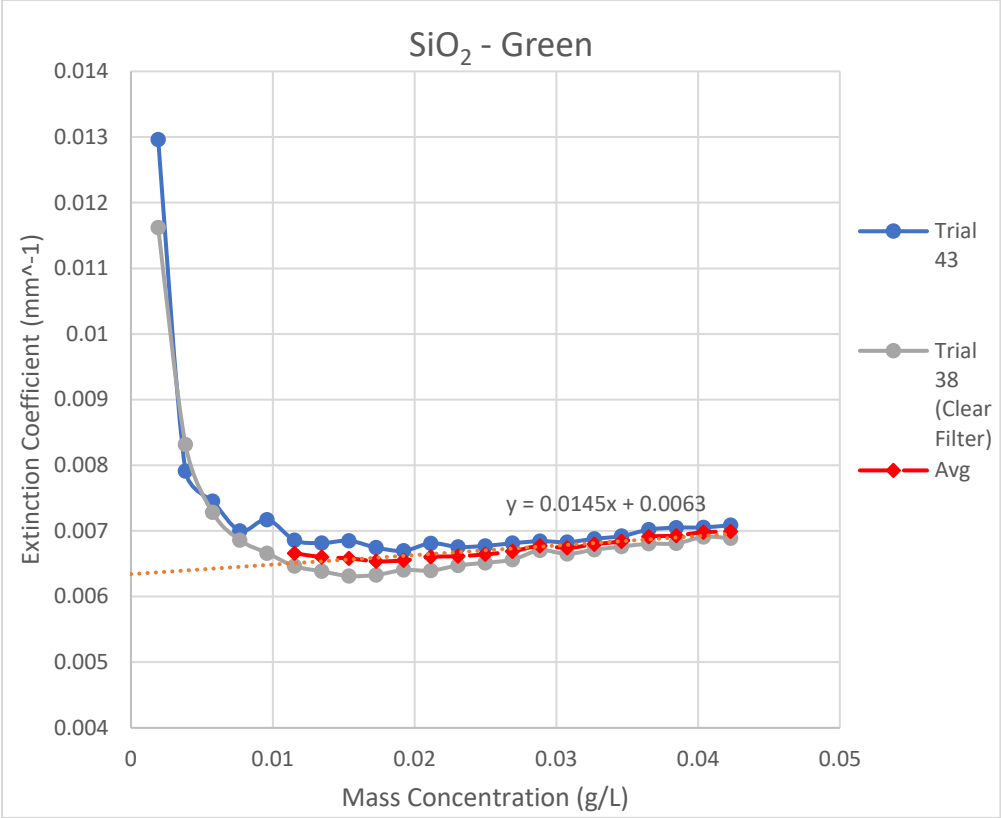

Figure 4.8 – SiO_2 at green wavelength.

For the green wavelength, one of the data sets was missing, so only two Trials are represented. An average was shown for the two data curves.

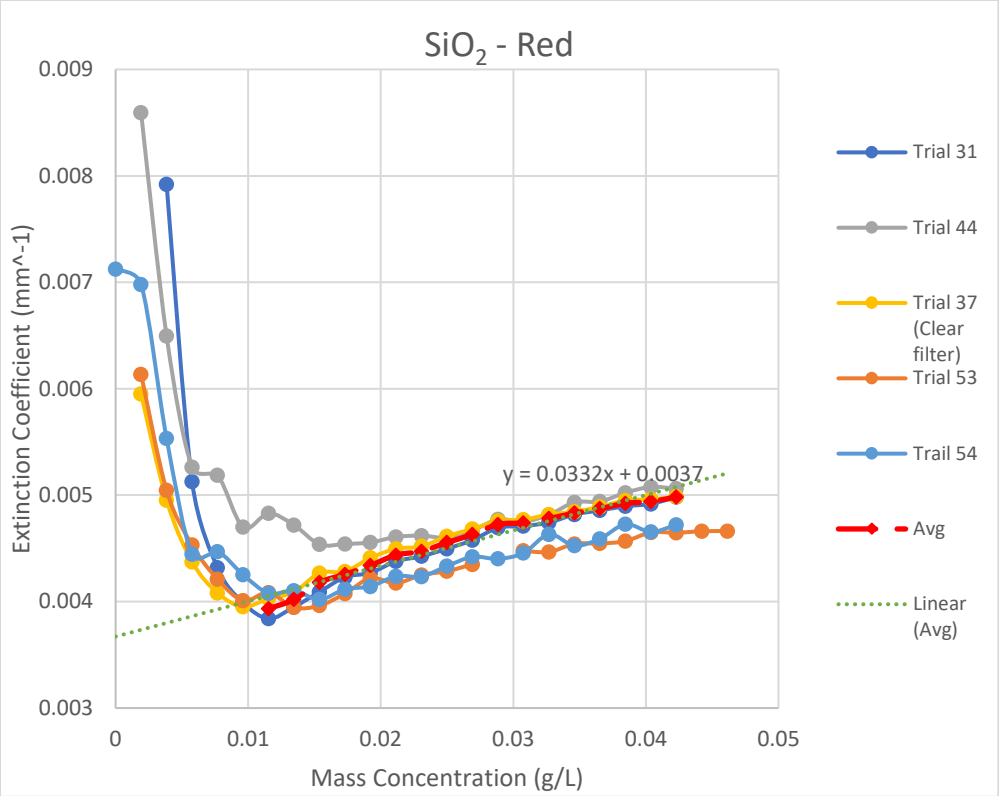

Figure 4.9 – SiO_2 at red wavelengths.

Much data was available for SiO_2 with the red laser. This data is plotted in Figure 4.9 above. Overall the data is closely grouped together. The average is shown in red.

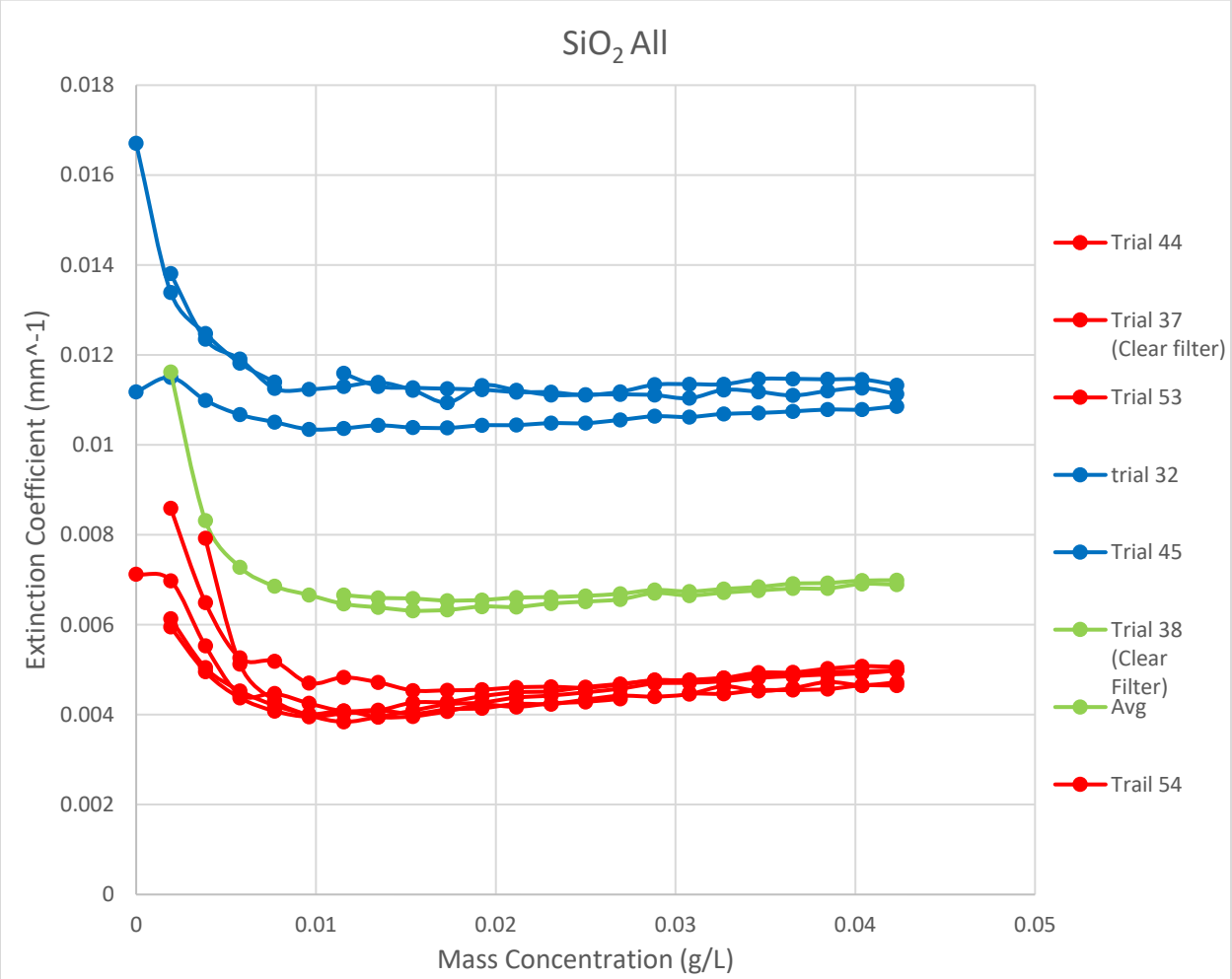

Figure 4.10 – Extinction Coefficients vs mass concentrations for SiO_2 particles at all wavelengths.

Once again all of the data was plotted together, as shown in Figure 4.10. Data from different wavelengths are notably grouped together, and separate from the other wavelength groups.

The data was also plotted for each wavelength for the two types of particles:

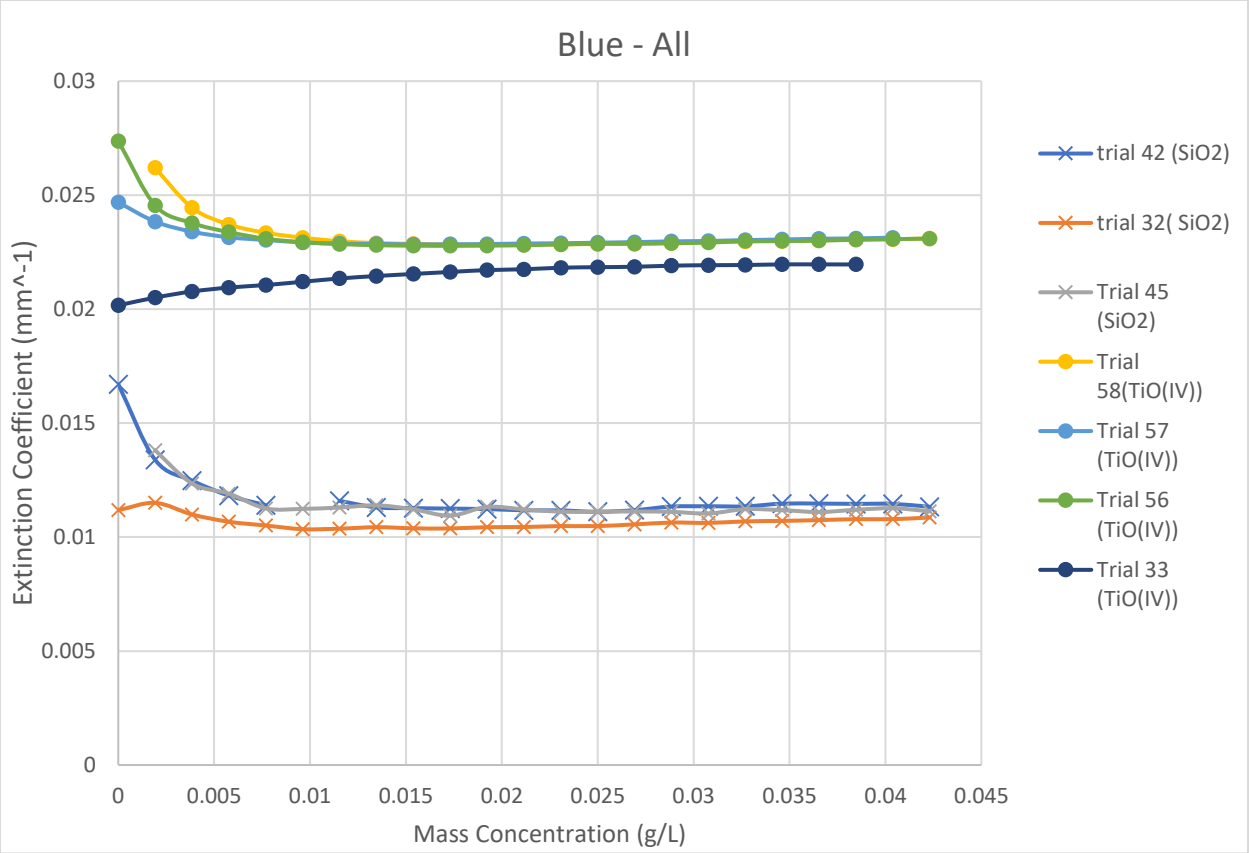

Figure 4.11 – Both particles at Blue wavelength.

Figure 4.11 shows all of the blue wavelength data plotted together. Data points marked with x's represent the SiO_2 data, while the dots represent the TiO_2 data. Ideally, the data would be plotted as a function of the number concentration of particles (defined as the number of particles per unit volume), rather than the mass concentration. However, due to difference in masses of the particles, the number concentrations represented varies greatly between the two particle types, so for ease of comparison, mass concentration is used.

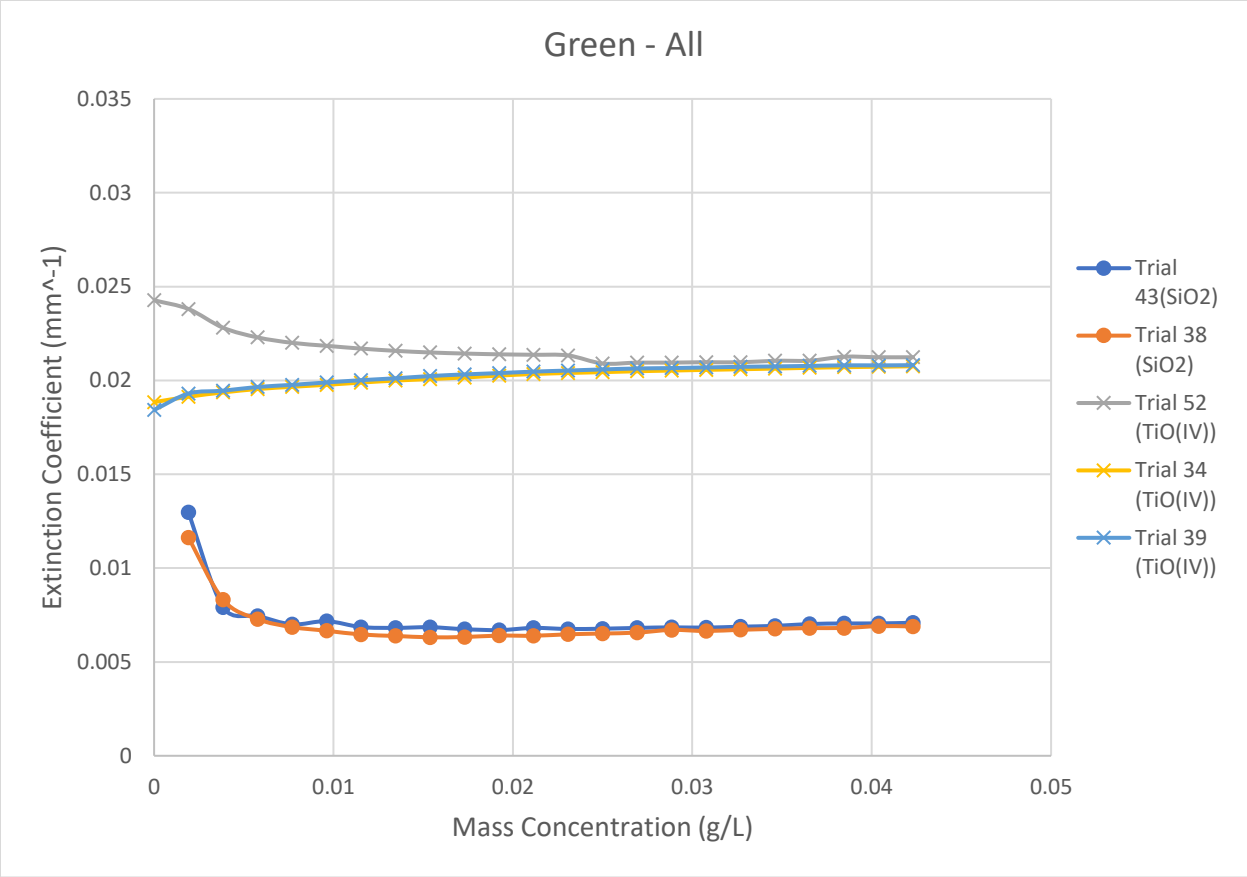

Figure 4.12 - Both particles at green wavelength.

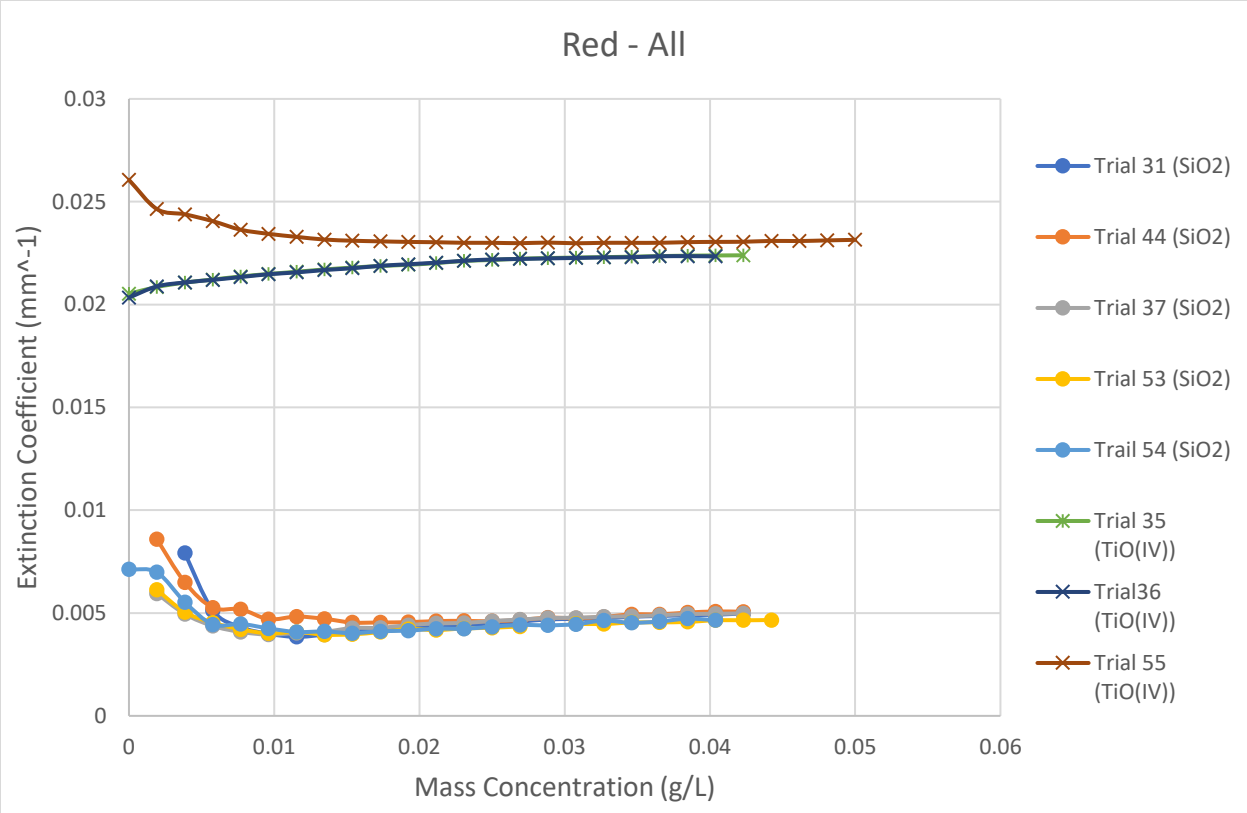

Figure 4.13 – Both Particles at red wavelength.

The extinction coefficient versus mass concentration graphs suggest that there is a definable relationship between the extinction coefficient and the mass concentration of particles (which, in turn, means there is a relationship with the number concentration as well). With the exception of a few outliers, the extinction curves are grouped very closely together. In Figure 4.10, we can see that the data for each wavelength is grouped together, and distinct from other wavelengths. In figure 4.6, there are a few outliers, but data for each wavelength is grouped together, and distinctly from other wavelengths again.

In the SiO_2 graphs, we again see that there is a general trend reinforcing the notion of a relationship between the particle density and extinction coefficient. In Figure 4.3.d, however, it appears that the blue laser extinction curves are higher than the other two wavelengths, and not as distinctly separated. The red and green wavelength extinction curves are again fairly similar, as with the TiO_2 particle experiments. It is also interesting that given the differences in incidence angle of early and later experiments, that there does not appear to be a great difference in the extinction coefficient as a result of this difference. This is unlike the TiO_2 data, where the difference in angle produced clearly different results. This could be a result of the lower refractive index of SiO_2 at these wavelengths. Additionally, as seen in the TiO_2 graphs, there is a larger difference in extinction coefficients between blue wavelengths and the others than with the SiO_2. This could be explained by fact that the difference in refractive index is greater in TiO_2 than with SiO_2. Comparing the SiO_2 graphs with the TiO_2 graphs, it is apparent that the TiO_2 has steeper slopes than SiO_2. This is also likely a result of the higher refractive indices of TiO_2 versus SiO_2 – if we compare the Mie backscatter efficiency (Q_{back}) values from Tables 3.1 and 3.2, we can see that the values for the TiO_2 particles are mostly higher than those of the SiO_2 particles for the bolded values (representing the particle radii used in the experiment).

In some of the graphs for the extinction versus mass concentration, we saw that some of the initial values were unusually high compared the rest of the values (such as in Figures 4.11 and 4.12). This high value is more likely attributed to the poor fit of the modelling curve at these concentrations, rather than an indication that the extinction has a large drop off then steady increase. Because there are very few particles in the system at the lower mass concentration levels, there are fewer objects to scatter light back to the camera. Therefore, that could be mistakenly interpreted as there being a high level of extinction occurring. Extinction values, logically, should start at a low value and then increase as the number concentration of particles in the system increases, as there are more scatterers present that block light from returning to the CCD.

Some of the curves for TiO_2 did start at a lower value and increased steadily. This behavior is closer to what would be expected. It was found that some of the experiments were conducted with an incidence angle of 35.0°, and some at 55.0° (discussed further in Chapter 5). It appears that the odd behavior occurred for trials with the higher incident angle at 55°. This suggests that, perhaps, future iterations of this experiment should be conducted with the higher incident angle. However, for the SiO_2 particles, it appears that the difference in incident angle did not have a major impact. All SiO_2 curves started with a high extinction value, but these decreased and increased again.

While this method appears to not consistently produce logical results at lower particle concentrations, it does appear to work well at higher levels. Given the consistency in the extinction coefficients at the higher concentration levels at each wavelength, for each particle type, models can be developed that can be used to extract particle concentrations in a system.

We can use the particle radii found by Szopa et. al. (2005) in conjunction with the refractive indices of Titan tholins measured by Khare and Sagan (1984) to find the efficiency

factors for tholins at different radii (assuming a spherical shape) in liquid methane in Table 6.1. These values could be used to help produce a model for Titan tholins.

Particle Radius (microns)	**Q factor**	**Blue**	**Green**	**Red**
r = 0.250	Q_{ext}	2.456	2.478	1.765
	Q_{sca}	3.112	2.744	1.845
	Q_{back}	0.155	0.193	0.089
r= 0.500	Q_{ext}	1.524	2.665	3.627
	Q_{sca}	2.515	3.153	3.792
	Q_{back}	0.079	0.126	0.131
r=0.750	Q_{ext}	1.271	1.343	2.316
	Q_{sca}	2.358	2.003	2.555
	Q_{back}	0.082	0.425	0.030
r=1.000	Qext	1.203	1.833	1.625
	Qsca	2.300	2.608	1.945
	Qback	0.017	0.623	0.969

Table 4.1 - Q Factors for Titan Tholins at each wavelength

It should be noted that the use of different liquid media will yield different Mie efficiency and extinction values. In this experiment, the medium used was water, with an assumed refractive index of 1.33. Different media will have different refractive indices, which would change the light wavelength in the medium, and result in different Q values, as these are functions of wavelength.

The modelling equation was used to examine data from Moores et al. (2011). Images of the LIDAR laser (533.0 nm) taken by the Stereo Surface Imager (SSI) were analyzed, adjusting the input parameters to account for the Martian conditions being studied. For example, the scattering efficiencies were $Q_{scat} = 2.04$ and $Q_b = 0.09$, and the laser power was 40 mW. The SSI had a field of view of 13.8° and the CCD was 1024x1024 pixels. Figure 4.14 shows an example fo one of the images analyzed.

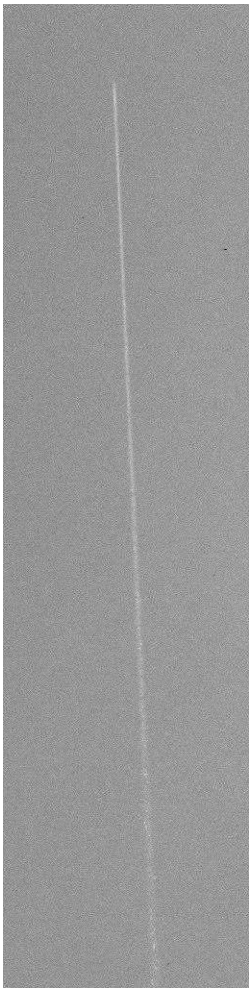

Figure 4.14 – Image of lidar laser from Phoenix SSI. *Courtesy Dr. John Moores.*

The following graphs (Figure 4.15) show the model vs the data, with error from Moores et al. (2011):

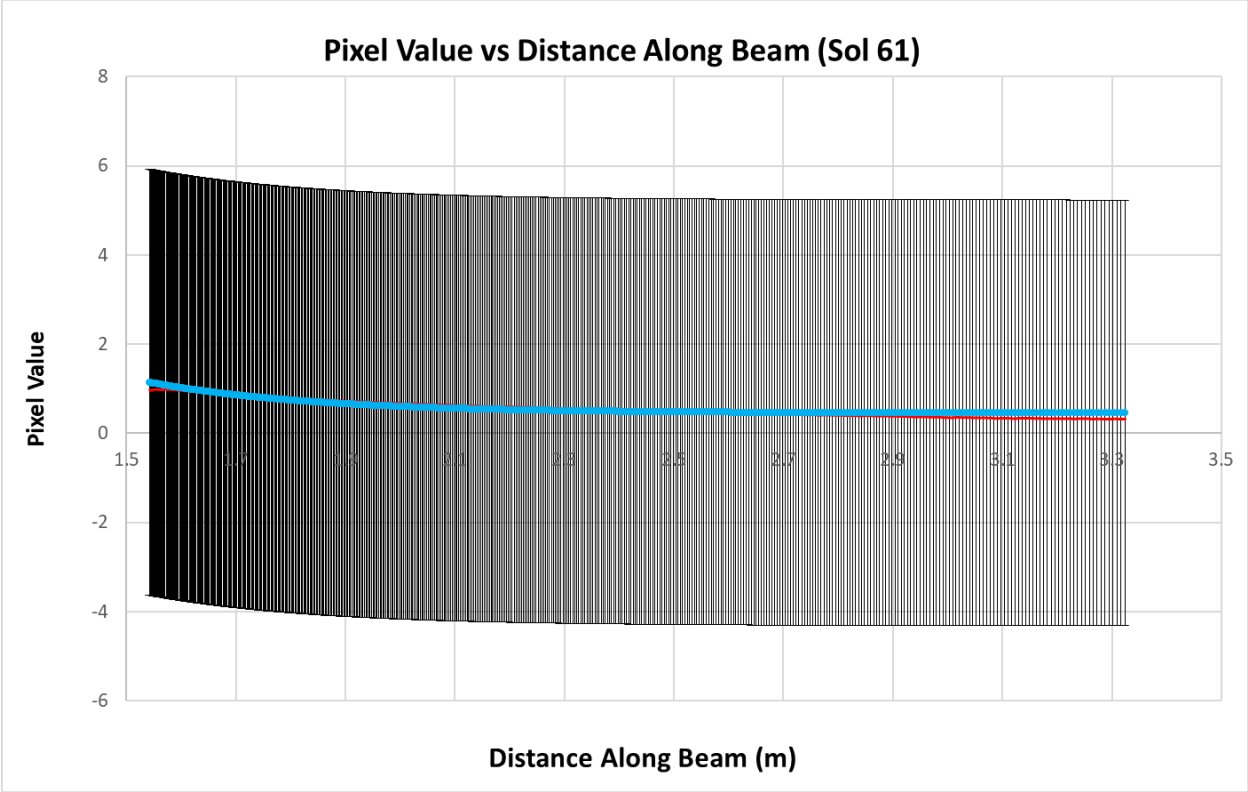
Pixel Value vs Distance Along Beam (Sol 61)
Pixel Value
8
6
4
2
0
-2
-4
-6
1.5
3.5
Distance Along Beam (m)

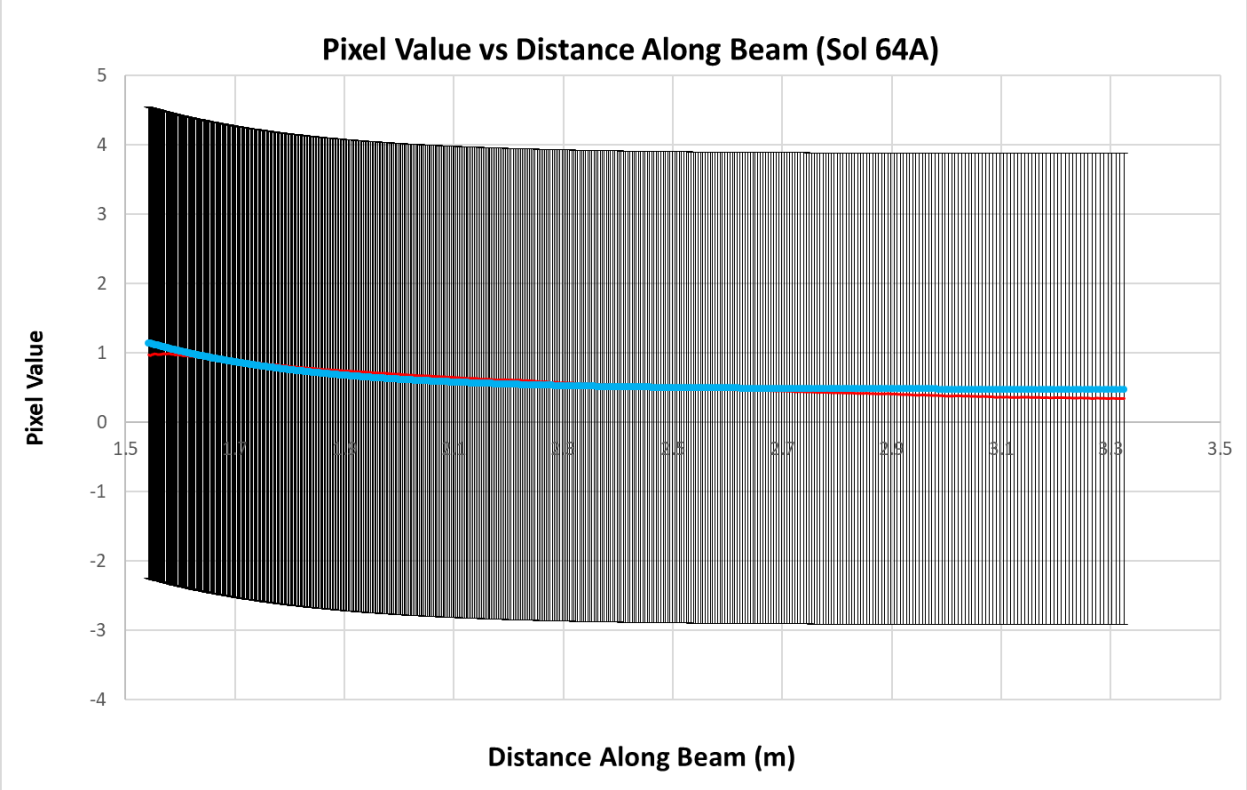
Pixel Value vs Distance Along Beam (Sol 64A)
Pixel Value
5
4
3
2
1
0
-1
-2
-3
-4
1.5
3.5
Distance Along Beam (m)

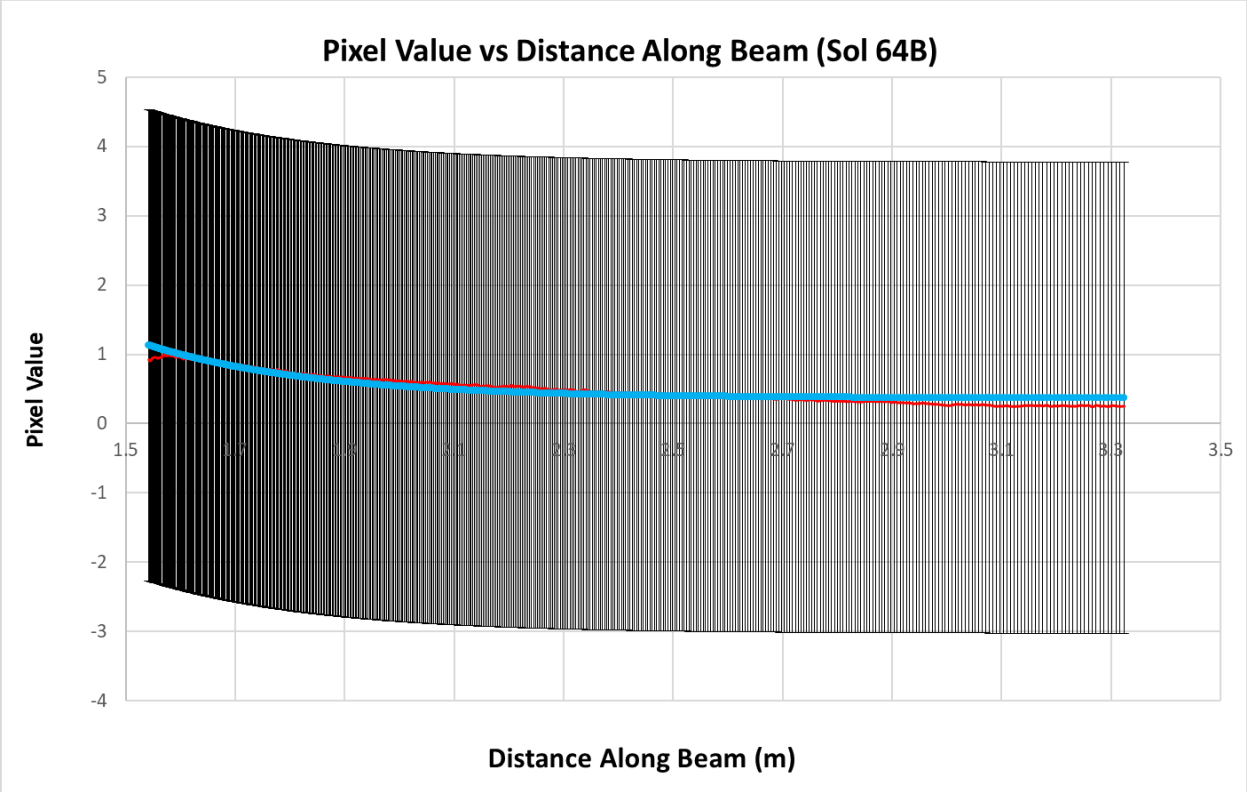
Pixel Value vs Distance Along Beam (Sol 64B)
Pixel Value
5
4
3
2
1
0
-1
-2
-3
-4
1.5
3.1
3.3
3.5
Distance Along Beam (m)

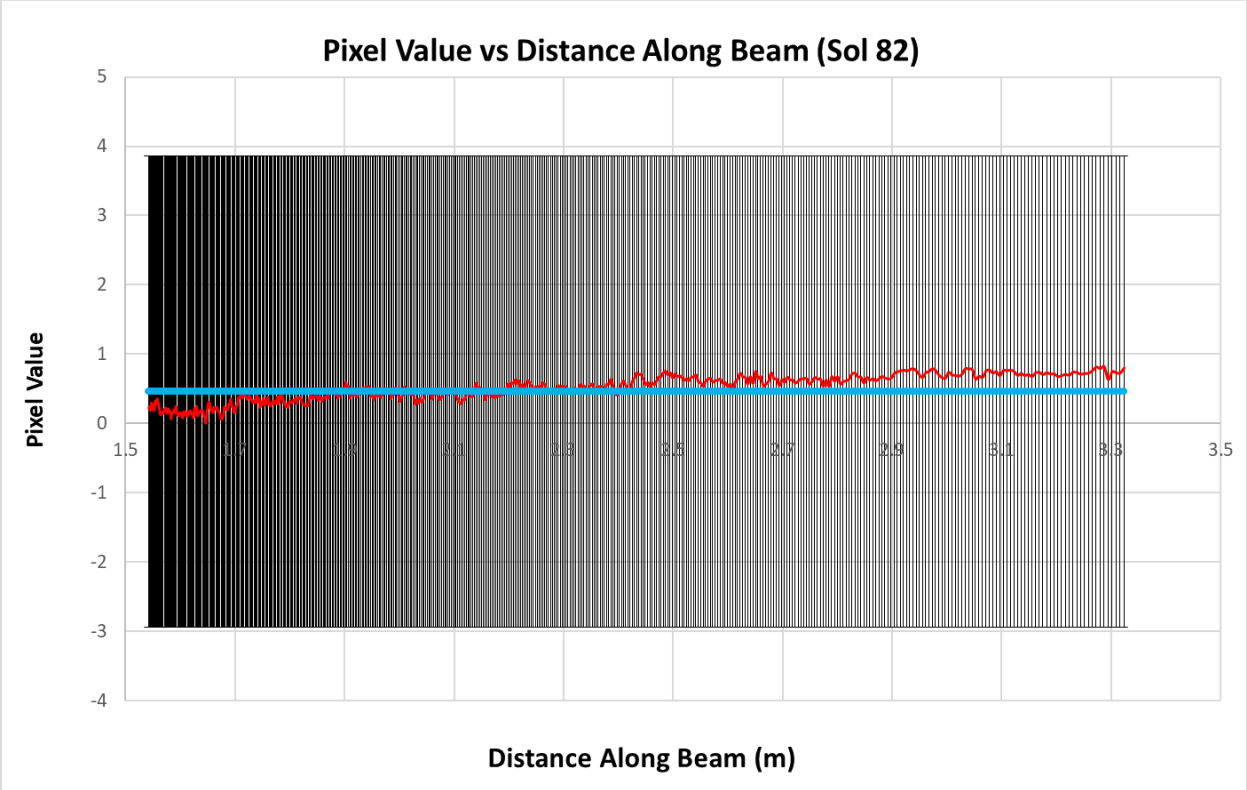
Pixel Value vs Distance Along Beam (Sol 82)
Pixel Value
5
4
3
2
1
0
-1
-2
-3
-4
1.5
3.1
3.3
3.5
Distance Along Beam (m)

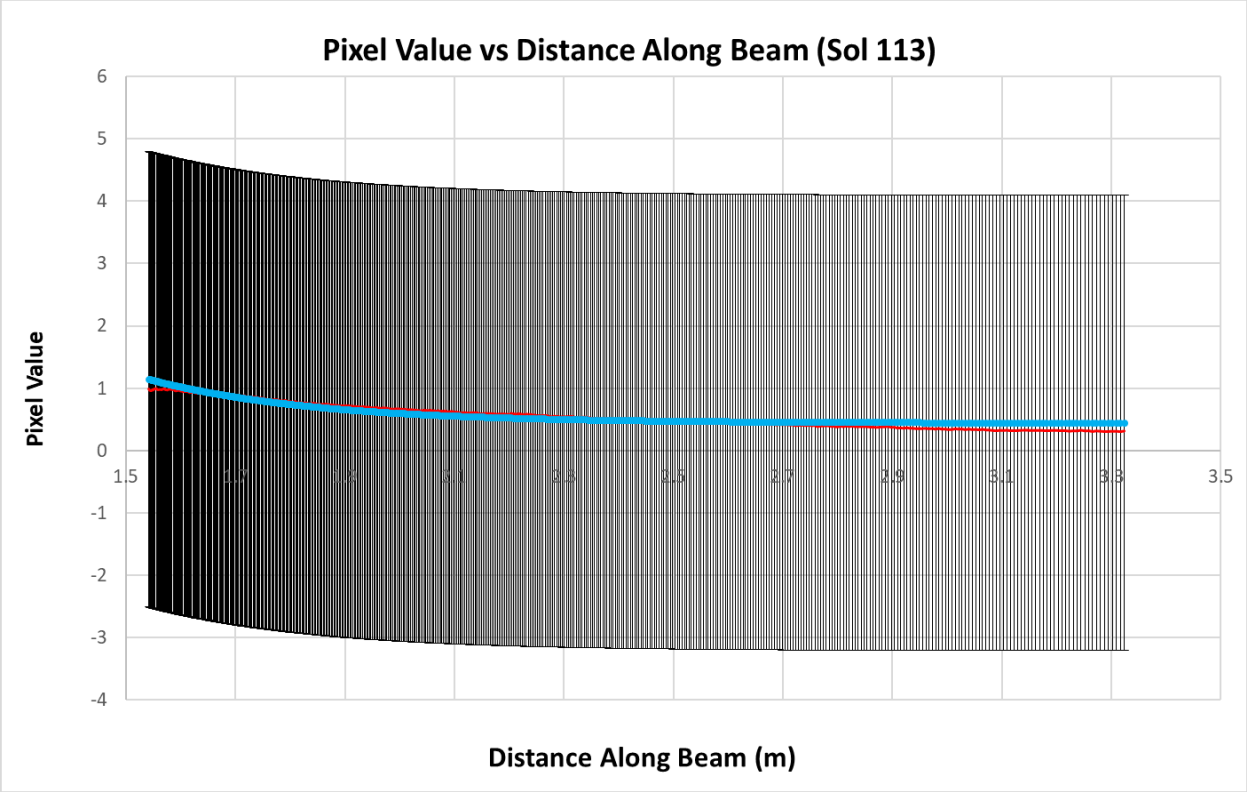

Figure 4.15 – Analysis of Images from Phoenix SSI. *A "sol" is a day on Mars.*

The error for these graphs is rather large. From these, we can see that the model appears to fit fairly reasonably. The extinction coefficients obtained by these graphs are shown in Table 4.4:

	Sol 61	Sol 64A	Sol 64B	Sol 82	Sol 113
Extinction Coefficient	1.676568	1.6851	1.645359	7.78622	1.671553

Table 4.2 – Extinction Coefficients from Phoenix SSI Images.

With the exception of Sol 82, it appears that the extinction coefficients are similar.

This research has made several contributions to the goal of measuring turbidity. First of all, it has been shown that a low-powered laser can be used to measure extinction coefficients, as a function of the number of particles in a system. This shows that the methodology explored could be a viable alternative for turbidity measuring technologies in a mission to Titan, one that could result in energy savings. It has also been shown that the wavelength and incidence angle of the laser are two important factors to consider – for example, Figure 4.10 shows that the output

extinction coefficients will vary with the laser wavelength. Figure 4.6 shows that for particles that have a higher refractive index, a lower incident angle should be used for more accurate measurements, particularly for lower concentrations of suspended particles. However, particles with lower refractive indices may experience poorer data quality at lower particle concentrations.

This experiment was limited to a water medium with two types of particles, with no absorption component to in the refractive index of the particles. The experiment was also conducted in a small aquarium tank, which limited some of the geometrical aspects of the experiment. An actual mission to Titan would not have some of these same geometrical constraints, and would be conducted in a liquid methane environment, looking for particles with a different refractive index. The Titan environment would be much colder than the environment in which this research was conducted. A system using a camera and a laser would need to be developed to withstand both conditions on Titan, as well as the cold and radiation encountered on the way to the Saturn system.

5. Sources of Error

5.1 Low Mass Concentration

In Figure 4.2, we can see that at very low mass concentrations, the fit of the modeling curve to the data is poor. As a result, in several of the extinction curve plots, the extinction value shown at low mass concentrations is counterintuitively high – for example, in Figure 4.5, the initial extinction for Trial 55 is above 0.025, then the curve drops to a lower value and begins to increase again.

5.2 Flat Field Images

During analysis, it was also found that some of the flat field images that were taken were not of a good quality as the lighting was uneven in the images, and in some instances, were difficult to use for the reduction of the data. Some of the flat field images were missing for earlier experiments as well. In an attempt to mitigate the issues with the flat field images, some of the data analysis for one experiment was done with an averaged flat field image from another trial. This may have caused some error due to any differences in the flat field images. For example, the lens of the camera may have had dust or a smudge that was not present for another experiment, meaning that the flat field image from another experiment may not be representative of the state of the lens of another experiment. However, one of the trials was analyzed using several different flat field images from various other trials, and the differences in output data were found to be negligible. Issues with the flat field images was also mitigated by ensuring that if any flat field images were used from a different experiment, that the alternative flat field image was taken with the same filter. When possible, the alternative flat field images used were taken at a time as close to the original experiment's time as possible. Dark field images did not appear to have any issues occur.

In several of the graphs seen previously, there are a few obvious outliers. These outliers are the data from experiments 33, 52, and 55. Original flat field images were missing for trial 33, and trial 55 had poor quality flat field images, and thus required the use of other flat field images. Trial 54 was conducted immediately after trial 53 and used the same filter; the camera was not turned off between the two trials, and thus additional flat field images were not necessary. However, the flat field images that had been taken for trials 54 and 55 yielded anomalous results. Further examination of the averaged flat field image suggested that the averaged images were poor quality and not usable for the data, and thus a different averaged flat field image was used. Since the reuse of flat field images were found to have a negligible impact on the output data, it is unlikely that the reuse of these were the cause for the outliers.

5.3 Mixing

Another possibility is that the error originated in the mixing of particles into the system. It is possible that some of the particles were not fully mixed into the beaker of water extracted from the system. If this were the case, then some of the particles may have settled at the bottom rather than being mixed homogenously into the system. Alternatively, the issue could have been with the mixing system itself; perhaps the pump used was not functioning as efficiently as it was previously.

5.4 Incidence Angle

The most likely explanation for the presence of these outliers relates to the incidence angle used during the experiments. An issue with the angle of the laser was discovered after conducting trials 46-51. The laser modules are mounted to an optical system with a beam splitter on a rotating mount that precisely sets the angle of the beam. This was set so that the beam splitter reflected the beam at 55 degrees from horizontal; however, after trial 51, it was found that the beam splitter was loose and not reflecting the beam at 55 degrees. The data from the few previous experiments (trials

46-51) was deemed unusable, as the angle of the beam could not be verified. Trials 42 through 45 were conducted with the verified beam angle.

Furthermore, it was discovered that the previous trials were conducted at a different angle. Trial 42 and onward were conducted with the angle of the laser 55 degrees from horizontal; that would mean the incidence angle for these experiments was 35 degrees. Earlier experiments were conducted at a 55 degree incidence angle (i.e. 55 degrees from vertical). This is possibly supported by the fact that the graphs of the early trials feature different slopes from those of the newer trials, but the slopes within each group are similar to each other.

6. Future Work

Due to the error in the incidence angle used, some of the data sets obtained are incomplete. Performing more experiments at both the 55 degree and 35 degree incidence angles to obtain a complete set can offer more insight and confirmation of the previously found results. Additionally, the experiment could be completed with a scatterer that has properties more similar to that of Titan tholins – particularly with a non-zero value for the imaginary component of the refractive index, which would indicate that absorption occurs as well. Ideally, a future experiment would be conducted with tholins suspended in liquid methane – a controlled experiment could produce results that would serve as a model for measuring tholins in Titan's methane lakes.

This research only examined single particle systems – future work could include systems containing various particle types. With the TiO_2 powder used, a mixture of different particle sizes was examined. A mixture of particles with different refractive indices would yield different, interesting results.

Another improvement to future experiments would be to factor in the exposure time. For this research, a single exposure time of 10 seconds was used throughout all runs of the experiment. However, with less backscattering occurring at lower particle concentrations, increasing the exposure time, and improving the modeling equation to account for this, could help to reduce the behavior seen in the extinction coefficient versus mass concentration graphs at lower particle concentrations.

Some other factors for conducting future experiments should be considered. For future experiments, it is important to ensure that the angle pf the laser is consistent. Ensure that all flat-field images have uniform lighting. Take appropriate measures, such as mixing particles into a beaker of water removed from the system, to make sure that the particles are homogenously mixed

in the system (also, make sure the particles used are insoluble in the liquid medium being used). Make sure the mounting device/method for all components are sturdy and restrict any free motion of the components (i.e. bumping the device won't set it out of place or change the field of view of the camera).

7. Conclusion

It has been shown that the extinction coefficient of light, due to turbidity, can be determined from the back scatter of light from a low-energy laser through image analysis. By relating the extinction coefficient to the mass of particles added to the system, it has been shown that the number concentration of a scattering particle in a medium can be estimated with a camera and a laser. However, it should also be noted that this method loses effectiveness at lower number concentrations – with few scatterers in the system, very little backscatter will occur, and may incorrectly suggest a high amount of extinction is occurring. Mie efficiency factors were also calculated for Titan tholins. These will be useful in future studies of tholins on Titan.

This method was developed with the goal of being used in Titan's methane lakes. However, this method would also be suitable for liquid bodies elsewhere, including Earth. This method can help to measure the number and concentration of pollutant particles in a system. It should also be noted that this method, as with Moores et. al., could be used to measure aerosols and particles suspended in air.

8. References

Alfa Aesaer. (2018, May 11). *Alfa Aesar*.

Andrews, D. G. (2000). *An Introduction to Atmospheric Physics.* New York: Cambridge University Press.

Barnes, J. W., & Brown, R. H. (2009). Shoreline Features of Titan's Ontario Lacus from Cassini/VIMS Observations. *Icarus*.

Barnes, J., Turtle, E., & Trainer, M. (2017). Dragonfly: a New Frontiers Titan Dune Lander. *Fifth Interplanetary Dunes Workshop.* St. George, Utah: LPI.

Bin Omar, A. F., & Bin MatJafri, M. Z. (2009). Turbidimeter Design and Analysis: A Review on Optical Fiber Sensors for the Measurement of Water Turbidity. *Sensors*.

Bird, M., Dutta-Roy, R., & Heyl, M. (2003). The Huygens Doppler Wind Experiment. In R. C.T., *The Cassini-Huygens Mission.* Dordrecht: Springer.

BMG LABTECH. (2017, DEC 19). *Nephelometer*. Retrieved from BMG LABTECH.

Bohren, C., & Huffman, D. (1983). *Aborption and Scattering of Light by Small Particles.* New York: Wiley.

Borucki, W., McKay, C., & Whitten, R. (1984). Possible production by lightning of aerosols and trace gases in Titan's atmosphere. *Icarus*.

Corrales, L. R., & Yi, T. D. (2017). Acetonitrile Cluster Solvation in a Cryogenic Ethane-Methane-Propane Liquid: Implications for Titan Lake Chemistry. *The Journal of Chemical Physics*.

Coustenis, A. (2008). *Titan: Exploring an Earthlike World.* Singapore: World Scientific Publishing Co.

Culham, J. (2004, March 1). *Bessel Functions of the First and Second Kind.* Retrieved from University of Waterloo.

DeVore, J. (1951). Refractive Indices of Rutile and Sphalerite. *Journal of the Optical Society of America*.

ESA. (2018, May 18). *SSP: Surface Science Package*. Retrieved from Cassini-Huygens.

Fischer, G., & Gurnett, D. (2011). The search for Titan lightning radio emissions. *Geophysical Research Letters*.

Fulchignoni, M., & Ferri, F. (2005). In situ measurements of the physical characteristics of Titan's environment. *Nature*.

Fulchignoni, M., Ferri, F., & Angrilli, F. (2002). The Characterisation of Titan's Atmospheric Physical Properties by the Huygens Atmospheric Structure Instrument (Hasi). *Space Scence Reviews*.

Hale, G.M., & Querry, M. (1973). Optical constants of water in the 200-nm to 200-µm wavelength region. *Applied Optics*.

Hanel, R., Conrath, B., & Flasar, F. (1981). Infrared Observations of the Saturnian System from Voyager 1. *Science*.

Hayes, A., Aharonson, O., & al., e. (2008). Hydrocarbon Lakes on Titan: Distribution and Interaction with a Porous Regolith. *Geophysical Research Letters*.

Hofgartner, J. D., & Lunine, J. I. (2012). Does Ice Float in Titan's Lakes and Seas? *Icarus*.

Hofgartner, J. D., Hayes, A. G., & al., e. (2016). Titan's "Magic Islands": Transient Features in a Hydrocarbon Sea. *Icarus*.

Hofgartner, J., Hayes, A., & al., e. (2014). Transient Features in a Titan Sea. *Nature Geoscience Letters*.

Horst, S. (2017). Titan's atmosphere and climate. *Journal of Geophysical Research*.

Horst, S. (2017). Titan's Methane Lakes. *Nature Astronomy*.

Imanaka, H., Khare, B., Elsila, J., et al. (2004). Laboratory experiments of Titan tholin formed in cold plasma at various pressures: implications for nitrogen-containing polycyclic aromatic compounds in Titan haze. *Icarus*.

Jet Propulsion Laboratory. (2016, August). *Saturn.* Retrieved from NASA.

Jet Propulsion Laboratory. (2017, January 10). *Titan's North*. Retrieved from NASA-JPL.

Jet Propulsion Laboratory. (2018, May 13). *Cassini Legacy*. Retrieved from NASA Jet Propulsion Laboratory.

Jet Propulsion Laboratory. (2018, May 18). *NASA*. Retrieved from Jet Proulsion Laboratory.

Jet Propulsion Laboratory. (n.d.). *RADAR.* Retrieved from Cassini Legacy.

Kerker, M. (1969). *The Scattering of Light and Other Electromagnetic Radiation.* New York: Academic.

Khare, B., & Sagan, C. (1984). Optical Constants of Organic Tholins Produced in a Simulated Titanian Atmosphere: From Soft X-Ray to Microwave Frequencies. *Icarus*.

Kirk, J. (1985). Effects of Suspensoids (Turbidity) on Penetration of Solar Radiation in Aquatic Ecosystems. *Hydrobiologia*.

Kohlhase, C., & Penzo, P. (1977). Voyager Mission Description. *Space Science Reviews*.

Kohn, C., & Dujko, S. (2018). Streamer Propogation in the atmosphere of Titan and other N2:CH4 or N2:02 mixtures. *arXiv*.

Kuiper, G. (1944). Titan: a Satellite with an Atmosphere. *Astrophysics Journal*.

Lane, A., Hord, C., & West, R. (1982). Photopolarimetry from Voyager 2: Preliminary Results on Saturn, Titan, and the Rings. *Science*.

Lebreton, J., Witasse, O., Sollazzo, C., et al. (2005). An overview of the descent and landing of the Huygens probe on Titan. *Nature*.

Lee, R., & Rast, W. (1997). *LIGHT ATTENUATION IN A SHALLOW, TURBID RESERVOIR.* Lake Houston, TX: U.S. Geological Survey.

Lesser, M. (2015). A Summary of Charge-Coupled Devices for Astronomy. *Publications of the Astronomical Society of the Pacific*.

Lewis, J. (1971). Satellites of the Outer Planets: Their Physical and Chemical Nature. *Icarus*.

Lindal, G., & Wood, G. e. (1983). The Atmosphere of Titan: An Analysis of the Voyager 1 Radio Occultation Measurements. *Icarus*.

Lorenz, R., & Mitton, J. (2002). *Lifting Titan's Veil.* Cambridge: Cambridge University Press.

Malitson, I. (1965). Interspecimen Comparison of the Refractive Index of Fused Silica. *Journal of the Optical Society of America*.

Markowicz, K. (2018). *Aerosol and Radiation Observatory.* Retrieved from University of Warsaw.

Martonchik, J. V., & Orton, G. S. (1994). Optical constants of liquid and solid methane. *Applied Optics*.

Mastrgiuseppe, M., Poggiali, V., et al. (2014). The Bathymetry of a Titan Sea. *Geophysical Research Letters*.

Mastroguiseppe, M., & Hayes, A. (2017). Bathymetry and Composition of Titan's Ontario Lacus derived from Monte Carlo-Based Waveform Inversion of Cassini RADAR Altimetry Data. *Icarus*.

Matson D.L., S. L. (2003). The Cassini/Huygens Mission to the Saturnian System. In R. C.T., *The Cassini-Huygens Mission* (pp. 1-58). Dordrecht: Springer.

Matzler, C. (2002). *MATLAB Functions for Mie Scattering and Absorption.* University of Bern: Institute of Applied Physics.

McDonald, G. D., Thompson, W. R., & Heinrich, M. (1994). Chemical Investigation of Titan and Triton Tholins. *Icarus*.

Mitri, G., & Coustenis, A. (2014). The exploration of Titan with an Orbiter and a lake probe. *Elsevier*.

Moores, J., & Komguem, L. e. (2011). Observations of Near-Surface Fog at the Phoenix Mars Landing Site. *Geophysical Research Letters*.

NASA. (2017, December 14). *The Pioneer Missions*. Retrieved from NASA.

Ness, N., Acuna, M., & Lepping, R. (1981). Magnetic Field Studies by Voyager 1: Preliminary Results at Saturn. *science*.

Niemann, H., Atreya, S., & Bauer, S. (2002). The Gas Chromotograph Mass Spectrometer for the Huygens Probe. *Space Science Reviews*.

NOAA. (2008). *Lecture 3. Optical Properties.* Retrieved from Geophysical Fluid Dynamics Laboratory.

Prahl, S. (2018, August). *Mie Calculator.* Retrieved from Oregon Medical Laser Center.

Sagan, C., Khare, B., & Lewis, J. (1984). Organic matter in the Saturn system. In T. Gehrels, & M. Matthews, *Saturn.* Tucson: University of Arizona Press.

Samuelson, R., & Hanel, R. (1981). The mean molecular weight and hydrogen abundance of Titan's atmosphere. *Nature*.

Santa Barbara Instrumnet Group. (2005, Fenruary 10). *Model ST-9XE CCD Imaging Camera*. Retrieved from SBIG.

Sekine, Y., Imanka, H., et al. (2007). The role of organic haze in Titan’s atmospheric chemistry I. Laboratory investigation on heterogeneous reaction of atomic hydrogen with Titan tholin. *Icarus*.

Smith, B., Soderblom, L., & Batson, R. (1982). A New Look at the Saturn System: The Voyager 2 Images. *Science*.

Smith, B., Soderblom, L., & Beebe, R. (1981). Encounter with Saturn: Voyager 1 Imaging Science Results. *Science*.

Spectral Instruments Inc. (2018, May 17). *What is a CCD?* Retrieved from Spectral Instruments Inc.

Stofan, E., Elachi, C., Lunine, J., Lorenz, R., et al. (2007). The Lakes of Titan. *Nature*.

Stofan, E., Lorenz, R., et al. (2013). TiME - The Titan Mare Explorer. *Aerospace Conference.* IEEE .

Szopa, C., Cernogora, G., et al. (2005). PAMPRE: A dusty plasma experiment for Titan's tholins production and study. *Elsevier*.

Tomasko, M. (1980). Premilinary Results of Polarimetry and Photometry of Titan at Large Phase Angles from Pioneer 11. *Journal of Geophysical Research*.

Tomasko, M., & Smith, P. (1982). Photomertry and Polarimetry of Titan: Pioneer 11 Observations and Their Implications for Aerosol Particles. *Icarus*.

Tomasko, M., Doose, L., & Smith, P. (1996). Descent imager/spectral radiometer (DISR) instrument aboard the Huygens Probe of Titan. *Cassini/Huygens: A Mission to the Saturnian Systems.* Denver: SPIE.

Turtle, E., Perry, J., Barbara, J., et al. (2018). Titan's Meteorology Over the Cassini Mission:Evidence for Extensive Subsurface Methane Reservoirs. *Geophysical Research Letters*.

Tyler, G., Eshleman, V., & Anderson, J. (1982). Radio Science with Voyager 2 at Saturn: Atmosphere and Ionosphere and the Masses of Mimas, Tethys and Iapetus. *Science*.

Tyler, G., Eshleman, V., Anderson, J., Levy, G., & Lindal, G. (1981). Radio Science Investigations of the Saturn System with Voyager 1: Preliminary Results. *Science*.

University of Arizona. (2018, May 19). *Surface Stereo Imager*. Retrieved from Phoenix Mars Mission.

Van de Hulst, H. (1957). *Light Scattering by Small Particles.* New York: Wiley.

Wall, S., & Hayes, A. (2010). Active Shoreline of Ontario Lacus, Titan: a Morphological Study of the Lake and its Surroundings. *Geophysical Research Letters*.

Whiteway, J., Daly, M., Carswell, A., Duck, T., Dickinson, C., Komguem, L., & Cooke, C. (2008). Lidar on the Phoenix mission to Mars. *Journal of Geophysical Research*.

Wiscombe, W. (1980). Improved Mie scattering algorithms. *Applied Optics*.

Zarnecki, J., McDonnel, J., & Green, S. (1992). A surface science packacge for the Huygens Titan probe. *Symposium on Titan* (pp. 407-409). ESA.

Appendices

A. MATLAB code for Image analysis

```
clc
clear all

flat_avg =
fitsread('C:\Users\escap\Documents\YorkU\Projects\trial56\flat_avg.FIT');
dark_avg =
fitsread('C:\Users\escap\Documents\YorkU\Projects\trial56\dark_avg.FIT');

%Import & correct Science data%
science_files_noParticles = dir('*.fit');
numfiles = length(science_files_noParticles);
%science_data_nopart = cell(1,numfiles);
%^opens all files ending with .fits in the given folder
for image=1:numfiles %for each image
    current_image_name = science_files_noParticles(image).name;
    science_data_nopart = fitsread(current_image_name); %read each fits file
   % figure('name','Uncorrected'), imagesc(science_data_nopart)

    A_1 = science_data_nopart - dark_avg; %correction of image
    B_1 = flat_avg - dark_avg;
    science_corrected_nopart = (A_1./B_1);

    science_corrected_norm = science_corrected_nopart -
min(science_corrected_nopart(:));
    science_corrected_norm = science_corrected_norm ./
max(science_corrected_norm(:));

%     for k=1:512 %for all columns in image (each image is 512x512 pixels)
%         for m=1:512 %for all rows
%             if(science_corrected_nopart(k,m) < 0) %if the value of a pixel
is less than zero
%                 science_corrected_nopart(k,m) = 0; %set that pixel to zero
%
%             end
% %             if(science_corrected_nopart(k,m) > 0.1) %if the value of a
pixel is less than zero
% %                 science_corrected_nopart(k,m) = 0; %set that pixel to
zero
% %             end
% %
science_corrected_nopart(k,m)=science_corrected_nopart(k,m)+.0001;
%         end
%     end

    %background subtraction
    bg_x = science_corrected_norm(50:80);
    bg_y = science_corrected_norm(450:480);

    bg = [bg_x bg_y];
```

```
    bg_avg = mean2(bg);

    science_corrected_norm = fliplr(science_corrected_norm);
    j = 185:235; %rows
    i = 1:512; %columns
    BeamOut2=zeros(length(j),length(i));
    BeamOut2=science_corrected_norm(512-j,i);

    BeamOut = mean(BeamOut2) - bg_avg; %take average of each column in beam,
correct for background
    BeamOut = fliplr (BeamOut);
   % science_corrected_nopart(512-j,i) = 1;
%          %flip image to represent original image
%     for j=1:512 %rows (all)
%         BeamOut(513-j)=0;
%         for i=275:300
%                 %science_corrected_nopart(j,i)
=science_corrected_nopart(j,i)+ 1;
%                 BeamOut(513-j)=science_corrected_nopart(j,i);
%         end
%     end



    %plot

    FigureName1 = (['Image',int2str(image)]);
    figure('Name', FigureName1,'NumberTitle','Off');

surf(1:length(science_corrected_norm(:,1)),length(science_corrected_norm(1,:)
):-1:1,science_corrected_norm)
    hold on
   % plot(r,c,'o')
    view(2)
    shading interp
    axis tight
    colorbar
    caxis ([0 .5])



    FigureName2 = (['Pixel Length',int2str(image)]);
    figure('Name', FigureName2,'NumberTitle','Off');
    plot(1:length(BeamOut),BeamOut)
    xlabel('Length (pixels)')
    ylabel('Pixel Value')


%    L = 203.2; %[mm] distance between camera center and laser origin
%    y_0 = 750.89; %[mm] distance from camera to laser termination point
%    gamma = 62.53/2; %1/2 of FOV
%    B = tand(y_0/L); %angle between camera axis and laser (at image
midpoint)
```

```
%    theta = 180-gamma-B; %angle between edge of FOV and laser beam
%
%
%    b = sind(B)*(y_0/(sind(theta))); %distance from camera to beam origin
(mm)
%    x_mid = sind(gamma)*(y_0/sin(theta));%distance on beam to image midpoint
%

    L = 228.6; %[mm] horizontal distance between laser point at surface and
laser termination point (9 inch)
    y_0 = 609.6; %[mm] distance from water surface to bottom (24 inch)
    gamma = 136.4/2; %1/2 of FOV
    B = tand(y_0/L); %angle of laser relative to horizontal

    x_length = 416.7;%sqrt((y_0^2)+(L^2));

    n = 1:length(BeamOut); %number of pixels
    pixel_angle = (gamma*2)/512; %angle of a single pixel
    alpha = pixel_angle*n; %angle between end FOV and pixel length
    alpha_a = alpha(1:256); %select data through the first half of the image
    alpha_b = alpha(end);

    pixel_length = x_length./numel(n); %length of pixels in Beamout

    x = pixel_length*n;

%     alpha = pixel_angle*n; %angle between end FOV and pixel length
%     alpha_a = alpha(1:256); %select data through the first half of the
image
%     alpha_b = alpha(end);
%     beta = 180-gamma-theta; %angle b/w beam and camera axis
%     phi =180-alpha_b-theta;%angle b/w beam and camera distance to beam
terminus
%
%
%     x = sind(alpha)*(y_0/sind(theta));
%
%     y = (sind(theta)).*(x./(sind(alpha))); %distance from camera pixel to a
point on the beam
%
%     P_0 = BeamOut(1);% Pixel Intensity of first point
% %     sigma =-(1./x).*log(P_0./BeamOut); %extinction of light per unit
length
% %     tao_x = sigma.*x; %optical depth (along x)
% %     tao_y = sigma.*y;%optical depth (along y)
%
% %     P_x = P_0*exp((-1)*tao_x); %light emitted toward camera
%
    BeamData(image,:) = BeamOut;
%
%
%

       FigureName3 = (['Length',int2str(image)]);
       figure('Name', FigureName3,'NumberTitle','Off');
       plot(x,BeamOut)
       xlabel('Length (mm)')
```

```
       ylabel('Pixel Value')
    % fitswrite
(science_corrected_nopart,['C:\Users\escap\OneDrive\Documents\YorkU\Projects\
LaserTurbidity\CameraPics\Set3\NoParticles\Corrected\nopart_corr' int2str(i)
'.FIT']); %saves the corrected files
     SciOut = science_corrected_norm;
     SciOut = 255.*SciOut./(max(max(SciOut))); %normalize
     filename =(['Output_corrected',int2str(image),'.GIF']);
     imwrite(cast(SciOut,'uint8'),filename,'GIF');
     filename2 =(['Output_corrected',int2str(image)]);
     fitswrite (science_corrected_nopart,[filename2 '.FIT']); %saves the
corrected files

end
```

B. Trials

Trial #	Laser	Particle
1	Green	SiO2
2	Green	SiO2
3	Green	SiO2
4	Green	SiO2
5	Green	SiO2
6	Green	SiO2
7	Green	SiO2
8	Green	SiO2
9	Green	SiO2
10	Green	SiO2
11	Green	SiO2
12	Green	SiO2
13	Green	SiO2
14	Green	SiO2
15	Green	SiO2
16	Green	SiO2
17	Blue	SiO2
18	Blue	SiO2
19	Green	SiO2
20	Red	SiO2
21	Red	SiO2
22	Blue	SiO2
23	Unknown	Unknown
24	Blue	SiO2
25	Blue	SiO2
26	Blue	SiO2

27	Blue	SiO2
28	Red	Fe2O3
29	Green	SiO2
30	Green	SiO2
31	Red	SiO2
32	Blue	SiO2
33	Blue	TiO2
34	Green	TiO2
35	Red	TiO2
36	Red	TiO2
37	Red	SiO2
38	Green	SiO2
39	Green	TiO2
40	Unknown	Unknown
41	Unknown	Unknown
42	Blue	SiO2
43	Green	SiO2
44	Red	SiO2
45	Blue	SiO2
46	Green	SiO2
47	Red	SiO2
48	Unknown	Unknown
49	Blue	TiO2
50	Blue	TiO2
51	Blue	TiO2
52	Green	TiO2
53	Red	SiO2
54	Red	SiO2
55	Red	TiO2
56	Blue	TiO2
57	Blue	TiO2
58	Blue	TiO2